Three-Dimensional Thermodynamic Observations in Supercell Thunderstorms from Swarms of Balloon-Borne Sondes

ELISSA A. BARTOS,[a] PAUL M. MARKOWSKI,[a] AND YVETTE P. RICHARDSON[a]

[a] *Department of Meteorology and Atmospheric Science, The Pennsylvania State University, University Park, Pennsylvania*

(Manuscript received 20 May 2021, in final form 6 March 2022)

ABSTRACT: This study analyzes aboveground thermodynamic observations in three tornadic supercells obtained via swarms of small balloon-borne sondes acting as *pseudo-Lagrangian* drifters; the storm-relative winds draw the sondes through the precipitation, outflow, and baroclinic zones, which are believed to play key roles in tornado formation. Three-dimensional thermodynamic analyses are produced from the in situ observations. The coldest air is found at the lowest analysis levels, where virtual potential temperature deficits of 2–5 K are observed. Air parcels within the forward-flank outflow are inferred from their equivalent potential temperatures to have descended only a few hundred meters or less, whereas parcels within the rear-flank outflow are inferred to have downward excursions of 1–2 km. Additionally, the parcels following paths toward the low-level mesocyclone pass through horizontal buoyancy gradients that are strongest in the lowest 750 m and estimated to be capable of baroclinically generating horizontal vorticity having a magnitude of 6–10 × 10^{-3} s^{-1}. A substantial component of the baroclinically generated vorticity is initially crosswise, though the vorticity subsequently could become streamwise given the leftward bending of the airstream in which the vorticity is generated. The baroclinically generated vorticity could contribute to tornado formation upon being tilted upward and stretched near the surface beneath a strong, dynamically forced updraft.

SIGNIFICANCE STATEMENT: Swarms of balloon-borne probes are used to produce the first-ever, three-dimensional mappings of temperature from in situ observations within supercell storms (rotating storms with high tornado potential). Temperature has a strong influence on the buoyancy of air, and horizontal variations of buoyancy generate spin about a horizontal axis. Buoyancy is one of the primary drivers of upward and downward motions in thunderstorms, and in supercell storms, horizontally oriented spin can be tipped into the vertical and amplified by certain arrangements of upward and downward motions. Unfortunately, the long-standing lack of temperature observations has hampered scientists' ability to evaluate computer simulations and the tornadogenesis theories derived from them. We find that significant spin could be generated by the horizontal buoyancy variations sampled by the probes.

KEYWORDS: Cold pools; Convective storms/systems; Convective-scale processes; Deep convection; Tornadogenesis; Severe storms; Tornadoes; In situ atmospheric observations

1. Introduction

Severe thunderstorms can be hazardous to both life and property because of their tendency to produce damaging winds, hail, and tornadoes. Supercell thunderstorms, in particular, are responsible for the majority of strong tornadoes and large hail (Smith et al. 2012) and, thus, are an important focus of severe storms research. Moreover, tornadogenesis within supercell thunderstorms has been one of the most studied problems in the severe storms community over the past 60 years. Extensive reviews on the subject have been written by Ludlam (1963), Rotunno (1993), Davies-Jones et al. (2001), Markowski and Richardson (2009), and Davies-Jones (2015).

Many numerical modeling studies have found that vertical vorticity next to the ground develops from the tilting of horizontal, baroclinically generated vorticity into the vertical (e.g., Klemp and Rotunno 1983; Rotunno and Klemp 1985; Davies-Jones and Brooks 1993; Trapp and Fiedler 1995; Adlerman et al. 1999; Markowski and Richardson 2014; Parker and Dahl 2015). Across the forward-flank precipitation region, a horizontal buoyancy gradient associated with precipitation and cool outflow baroclinically generates horizontal vorticity along descending air parcel trajectories (e.g., Davies-Jones and Brooks 1993; Markowski and Richardson 2014). The horizontal vorticity within the rain-cooled air parcels can develop a vertical component via tilting, either while parcels are descending (Davies-Jones and Brooks 1993; Adlerman et al. 1999; Parker and Dahl 2015) or as parcels are ascending into the overlying, rotating, dynamically driven updraft (Rotunno et al. 2017; Boyer and Dahl 2020). The upward-directed, dynamic vertical perturbation pressure gradient force (VPPGF) accelerates these negatively buoyant, vorticity-bearing parcels upward, thereby also stretching the near-surface vertical vorticity (e.g., Markowski and Richardson 2014; Parker and Dahl 2015; Davies-Jones 2015; Guarriello et al. 2018). The VPPGF needs to be strong enough to overcome the negative buoyancy of the vorticity-rich parcels in the cold pool so that the parcels can be accelerated upward (e.g., Markowski and Richardson 2014; Parker and Dahl 2015). In these studies, tornadogenesis occurs if the predominantly baroclinic vorticity (i.e., vorticity with baroclinic origins) can undergo sufficient stretching after being tipped into the vertical.

Although the numerical-simulation evidence for the aforementioned baroclinic mechanism of tornadogenesis is legion,

---

Corresponding author: Elissa A. Bartos, eas558@psu.edu

DOI: 10.1175/MWR-D-21-0122.1

1) the baroclinic mechanism has never been fully confirmed in observations and 2) some recent simulations employing a semi-slip (i.e., bulk drag) lower boundary condition have cast doubt on the relative importance of the baroclinic mechanism (Schenkman et al. 2014; Roberts et al. 2016; Yokota et al. 2018). With respect to point 1, scattered observational evidence has been obtained in recent decades. Mobile mesonets (Straka et al. 1996; Waugh and Fredrickson 2010) and StickNets (Weiss and Schroeder 2008) have detected both baroclinity and relatively small negative buoyancy in tornadic supercells and larger negative buoyancy in nontornadic supercells (e.g., Markowski et al. 2002; Shabbott and Markowski 2006; Grzych et al. 2007; Hirth et al. 2008; Markowski et al. 2012a,b; Weiss et al. 2015), but unfortunately such observations are limited to the surface, and only where there are roads. Dual-Doppler wind syntheses have revealed vortex lines that arch upward out of supercell cold pools in the hook-echo region, with the horizontal projections of the vortex lines being aligned with the likely orientation of baroclinically generated horizontal vorticity (Markowski et al. 2008, 2011; Marquis et al. 2012; Kosiba et al. 2013; Markowski et al. 2018a). These vortex line characteristics are at least consistent with the baroclinic mechanism, though vorticity budgets along trajectories have been unavailable owing to a lack of thermodynamic observations. Dual-Doppler observations also have revealed profound differences in the trajectories that pass through supercell cold pools and subsequently reach the near-surface mesocyclone region of the storms, with cold-pool parcels being abruptly accelerated upward in tornadic storms (i.e., the rain-cooled, vorticity-rich parcels are lifted) but undercutting the overlying updraft in nontornadic supercells (i.e., failing to be lifted) (Markowski et al. 2011, 2012a). Again, without accompanying three-dimensional (3D) thermodynamic data, the vorticity budgets and buoyancy forces were unknown. Additionally, retrievals of buoyancy from dual-Doppler wind fields (e.g., Gal-Chen 1978; Brandes 1984a; Hane and Ray 1985; Hauser et al. 1988) have unfortunately been found to be too error-prone to be useful for vorticity budget calculations in supercell storms (Majcen et al. 2008).

With respect to point 2, numerical simulations of supercell storms performed in the twentieth century, and even the vast majority performed so far in the twenty-first century, have employed a free-slip lower boundary condition (Klemp and Wilhelmson 1978). Many of these simulations also have employed warm rain microphysics schemes (e.g., Klemp and Rotunno 1983; Rotunno and Klemp 1985; Davies- Jones and Brooks 1993; Adlerman et al. 1999), which are known to produce excessively cold outflow in proximity to supercell updrafts (e.g., Gilmore and Wicker 1998; Rasmussen and Straka 1998). Thus, it is possible that such simulations might have been prone to favor the baroclinic mechanism of tornadogenesis (or at least near-surface vertical vorticity amplification, given that tornadoes themselves are generally unresolvable in supercell simulations). In relatively recent supercell simulations by Schenkman et al. (2014), Roberts et al. (2016), and Yokota et al. (2018) employing more sophisticated microphysics schemes and a semi-slip lower boundary condition, horizontal vorticity generation by surface friction, with subsequent tilting and stretching, has been implicated in the formation of tornado-like vortices in the simulated storms. However, in addition to microphysics parameterization uncertainties, uncertainties also abound with respect to the appropriateness of assumptions involved in the formulation of the semi-slip lower boundary condition (Markowski 2016; Markowski and Bryan 2016; Wang et al. 2020).

The need for 3D thermodynamic observations within supercell storms is strongly implicated in the preceding two paragraphs. Remote sensing platforms (e.g., radiometers, Raman lidars), whether ground-based, airborne, or spaceborne, are not particularly useful given the inability to penetrate clouds and precipitation, and relatively long times required to complete a scan. Also, as explained above, dual-Doppler-based retrievals of buoyancy are currently unreliable, with the large sensitivity of the retrievals to observation errors and boundary conditions being the main issues (Majcen et al. 2008). Dropsondes are not a particularly good candidate either, given their expense (particularly when considering the cost of the mother aircraft), FAA restrictions over land, and the difficulty in flying the mother aircraft through the parts of the storm where the drops would be needed [see Markowski et al. (2018b), hereafter MRRP18, for additional details]. More recently, uncrewed aeronautical vehicles/systems (UAVs/UASs) have obtained aboveground observations within supercells (e.g., Houston et al. 2016; Frew et al. 2020). However, UAV use in the critical forward-flank precipitation region is challenging if not impractical, especially in the region near the mesocyclone, where visibility is extremely limited and high winds, turbulence, and large hail are present.

MRRP18 demonstrated a novel approach to obtaining aboveground thermodynamic observations by launching a small "swarm" of balloon-borne sondes into two supercells in May 2017. Two helium-filled balloons were attached to each sonde. After ascending to some separation altitude, most often set to 500–1500 m, one of the balloons was released, leaving behind an approximately neutrally buoyant sonde supported by the remaining balloon (at least in precipitation-free conditions), resulting in what was termed a *pseudo-Lagrangian* drifter. The ascent rate was typically 3–5 m s^{-1} in precipitation-free conditions, and following the release of one of the balloons, the vertical velocity tended to range from 0 to 2 m s^{-1} in precipitation-free air. Once in the precipitation of the storm (and once one balloon had been released), sonde vertical velocities ranged from several meters per second downward to slightly positive, depending on the strength of the storm-scale downdrafts and precipitation intensity (water that accumulates on the balloon, as well as the momentum transferred from falling raindrops to the balloon, contribute to negative vertical velocity). Though the balloon-borne sondes were not steerable like UAVs, in releasing them from a strategic location ahead of the storm on the southern edge of the forward-flank precipitation region, the storms' internal wind fields drew the sondes through key areas within the storms. The most useful sonde paths were those that passed through the forward-flank precipitation region and, ultimately, around the northern flank of the low-level mesocyclone.

The present study expands upon the MRRP18 study by deploying much larger swarms of sondes (≈30–50 sondes per storm), sufficient for producing gridded 3D thermodynamic analyses in three tornadic supercell thunderstorms intercepted in May 2019. Section 2 describes the data collection and analysis methods, section 3 contains an overview of the storm intercepts, section 4 presents the analyses, and section 5 provides a summary of the findings and a discussion of future work.

2. Methodology

a. Data collection

The tornadic supercells were intercepted on 17 May in southwestern Nebraska, 20 May in southwestern Oklahoma, and 23 May in the northeastern Texas Panhandle. The data collection was coordinated with the Targeted Observations by Radars and Unmanned Aircraft Systems (UAS) of Supercells (TORUS) field campaign. All of the storm environments were favorable for tornadoes, with the soundings exhibiting substantial convective available potential energy (CAPE), large low-level and deep-layer vertical wind shear, and high-relative-humidity boundary layers. The particulars of each intercept are described in section 3.

The balloon-borne sondes are the same as utilized by MRRP18. The sondes, commercially known as "Windsonds," are manufactured by Sparv Embedded, a small company based in Linköping, Sweden. The sondes are roughly the size of a small coffee cup, have a total mass of 12.4 g (including the 2.4-g battery), and measure temperature, relative humidity (RH), pressure, and global positioning system (GPS) latitude, longitude, and altitude above mean sea level (MSL). Errors for temperature, RH, and atmospheric pressure are, respectively, 0.3°C, 5%, and 0.3–0.5 hPa. Response times for temperature, RH, and atmospheric pressure are ~5, ~8, and ~0.04 s, respectively. It would be difficult to quantify possible wet-bulbing contamination, but we suspect it was limited because discontinuities were not observed in the temperature data. Moreover, the sondes, once wetted, typically remain in precipitation and nearly saturated air for the remainder of their flights, and the small sonde-relative air velocities (most likely 1–3 m s^{-1}) also would limit evaporative cooling. Wind velocity is obtained from the GPS directly. The sondes use "time-division multiple access" (TDMA) to share a single frequency; thus, the rate of data transmission from the sondes is limited by the number of sondes that are in flight. The tracking software was configured to allow up to 100 sondes to be tracked simultaneously, an improvement from 17 sondes per receiver as in MRRP18. This updated system allowed data to be collected approximately every 15 s. Communications between the sondes and receiver typically are maintained for 45–60 min (the battery lifetime) and out to ranges of 50–75 km, depending on line-of-sight.

In addition to the increased capability to track sondes simultaneously, the other difference relative to the MRRP18 deployment was the use of a variety of balloon types to achieve a greater diversity of trajectories through the storms. A mix of single-balloon and two-balloon sondes was used, with the latter featuring the release of one of the balloons at a predetermined height as in the MRRP18 deployment. Moreover, a mix of latex and Mylar balloons was used, with sizes ranging from 12 to 24 in. (~30.5 to 61.0 cm) in diameter, with larger balloons being used when the anticipated flight path was expected to encounter heavier precipitation rates. Experiments in controlled settings indicated that even a small, 12-in. (~30.5-cm) balloon could take on over 20 g of water, implying significant negative buoyancy for the balloon plus sonde, given a 12.4-g sonde mass.

Regarding the use of Mylar balloons, in principle they could afford some advantages over latex balloons. Given that they are constant-volume balloons (i.e., they do not expand as they rise), a balloon size could be found to yield neutral buoyancy at a pressure level favorable for one's observing needs, thereby obviating the need for the two-balloon approach used by MRRP18. Another possible advantage of Mylar balloons is the fact that they are much less porous than latex. As a result, Mylar balloons could be pre-inflated many hours, if not days, prior to a mission, with up to a few dozen pre-inflated balloons being stored in a large van. There are risks in pre-inflating latex balloons, given their porosity and the fact that it rarely is certain that there will be a targetable storm even just a few hours prior to a deployment. It is not possible to carry-over pre-inflated latex balloons to another day in the event that no targetable storms are identified. Not needing to inflate Mylar balloons during a storm intercept, and also only needing to attach a single balloon (as opposed to two balloons) to each sonde, could reduce the time between launches, which translates into more launches and improved sampling.

In practice, however, precipitation accumulation on the balloon is a "wild card," making it practically impossible to achieve neutral buoyancy throughout a flight through precipitation even with constant-volume balloons. Moreover, in our experience, the rapidity with which sondes can be launched is not so much a function of the time it takes to inflate balloons and attach them to sondes, but rather the time needed to obtain a GPS lock with our system (though we have some ideas for how to improve this in future deployments). Last, Mylar is much less environmentally friendly than latex. As in the MRRP18 deployments, the sondes were launched from positions 0–20 km upwind of the storm's forward-flank precipitation region, where upwind is with respect to the low-altitude storm-relative winds, which were estimated from the observed storm motion and either an observed or model-forecast hodograph. Thus, launch locations tended to be east or northeast of the forward-flank precipitation, such that sondes were drawn through the storms' precipitation and downdraft regions (i.e., the most scientifically interesting regions), sampling the coveted thermodynamic fields along the way. In the May 2019 deployments described herein, launches were performed by two three-person teams in vans spaced 10–15 km apart.

In summary, the May 2019 deployments experimented with a range of balloon types and sizes, yielding a wide variety of ascent rates in precipitation-free or light-precipitation conditions on the leading edge of the storms, and a variety of descent rates within heavier precipitation. As a result,

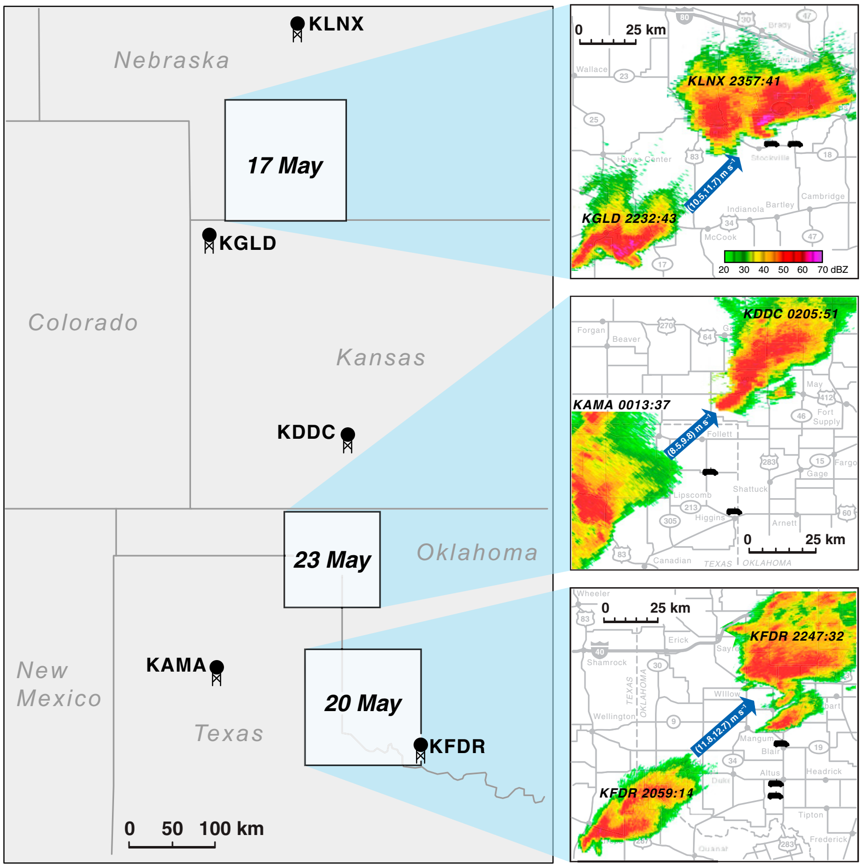

FIG. 1. An overview map of the 17, 20, and 23 supercell cases. In each inset, the vans' deployment locations are indicated by van icons, WSR-88D reflectivity imagery is shown at times near the beginning and end of the deployment period, and the mean storm motion is indicated by the blue arrow.

relatively dense sampling of the 3D thermodynamic fields was obtained in the lowest ~2 km by the ≈30–50 sondes flown through each storm.

b. *Data analysis*

The first analysis step was to map quality-controlled data to storm-relative coordinates using a time-to-space conversion (Fujita 1955). Each reference time coincides with a 0.5° elevation scan from the nearest Weather Surveillance Radar-1988 Doppler (WSR-88D). The reference times were chosen based on consideration of the difference in time between observations and the reference time (Δt) and radar beam height. Generally, we strove to minimize $|\Delta t|$ in the mesocyclone and rear-flank regions, which are the regions most likely to be unsteady, but $|\Delta t|$ considerations were balanced with a preference for lower beam heights (shorter ranges) over higher beam heights (longer ranges). The mean storm motion ($\mathbf{c}$) over the period in which sondes were airborne within the storm was determined by tracking the midlevel mesocyclone. Although data were collected over a ~1.5–2.0-h time period, the $|\Delta t|$ for most observations in the analyses is generally less than 60 min. Storm-relative, horizontal position errors can therefore be as large as a few kilometers, both from violations of Taylor's (1938) hypothesis and storm motion estimate errors (e.g., a 1 m s^{-1} error in the estimated storm motion introduces a 3.6-km sonde position error for a 60-min difference between the observation time and reference time).

The second analysis step was to interpolate the data to a Cartesian grid. The horizontal and vertical grid spacings are 500 m and 125 m, respectively, in all cases. The base of the grid [i.e., 0-m altitude above ground level (AGL)] corresponds to the altitude MSL of the lowest van in each case (the terrain is fairly flat in the regions of all three storm intercepts). Unless otherwise specified, all heights for both gridded and raw data in each case are defined with respect to the base of the grid. A one-pass, anisotropic Barnes (1964) objective analysis scheme was used for the interpolation. The data spacing in the horizontal is much less along sonde trajectories than across sonde trajectories. Given the approximately 15-s interval between data records and a characteristic storm-relative sonde horizontal velocity of 10 m s^{-1}, the horizontal data

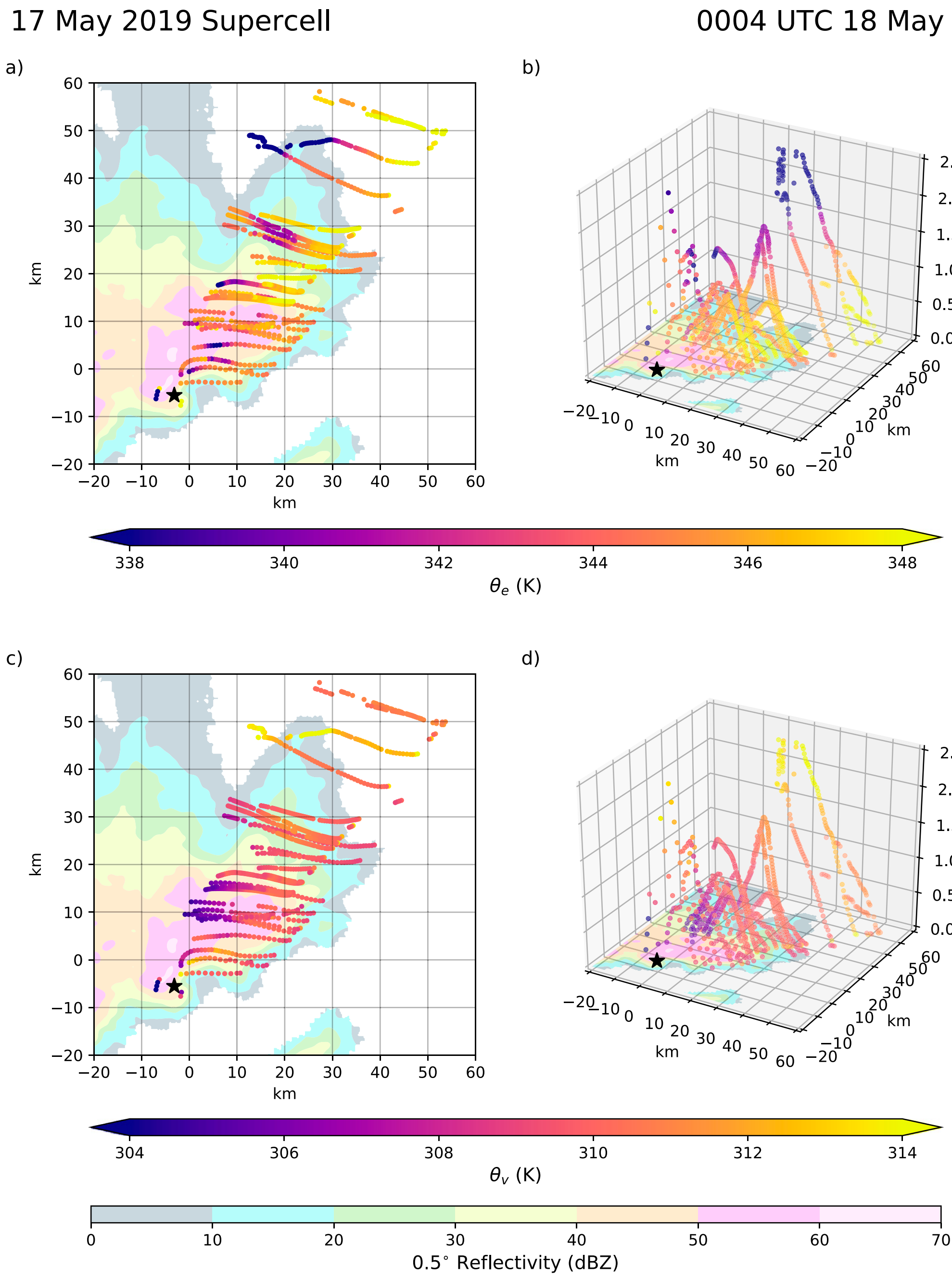

FIG. 2. Observations of (a),(b) θ_e and (c),(d) θ_v along the balloon-borne sondes' storm-relative trajectories in the lowest 2.5 km through the 17 May 2019 tornadic supercell. Horizontal plan views are shown in (a) and (c), and 3D perspectives from the southeast are shown in (b) and (d). The time-to-space conversion uses $\mathbf{c} = (10.5, 11.7)$ m s^{-1} and a reference time of 0004 UTC 18 May. The smoothed KLNX reflectivity field (lowest scan) is also shown. The location of the midlevel mesocyclone, which is determined from 0.5° elevation WSR-88D velocity data that intersect the storm at ~2.5 km above radar level, is indicated by a black star.

spacing along sonde trajectories is ~150 m. The horizontal data spacing across sonde trajectories is primarily governed by the launch frequency and storm motion. Given a ~60-s average launch interval and characteristic storm motion of 15 m s^{-1}, the horizontal data spacing across sonde trajectories would be ~900 m. The coarser of these two length scales guided the choice of the horizontal Barnes smoothing parameter, $\kappa_x = \kappa^* L_x^2$, where κ^* is a nondimensional smoothing parameter and L_x is a representative data spacing. Using $\kappa^* = (1.33)^2$ (Pauley and Wu 1990) and $L_x = 0.9$ km results in

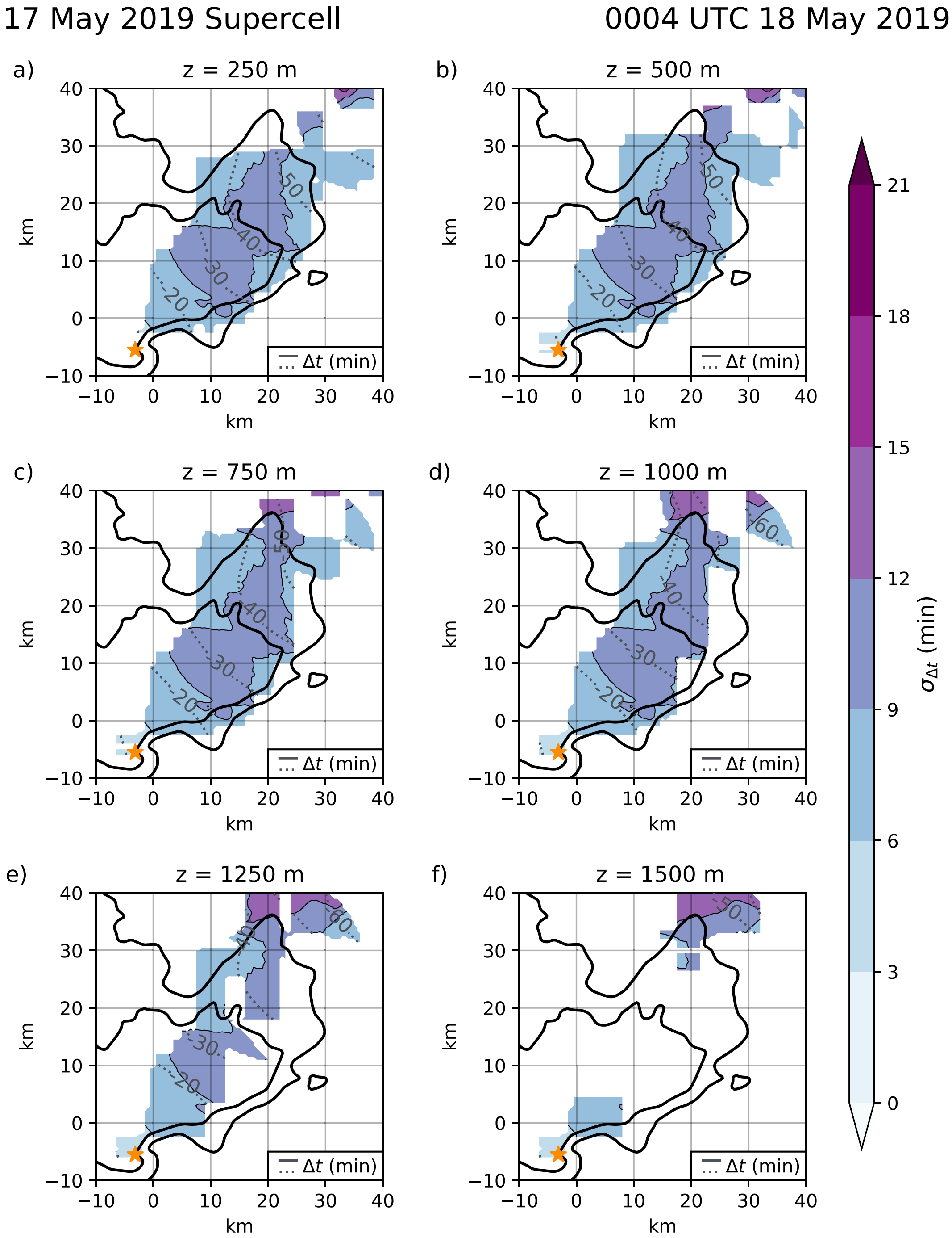

FIG. 3. Horizontal cross sections of smoothed time differences between observation times and the 0004 UTC 18 May reference time (Δt; black contours; min) and the standard deviation of unsmoothed Δt of the observations influencing each grid point ($\sigma_{\Delta t}$; color shading; min) in the 17 May 2019 supercell at (a) 250, (b) 500, (c) 750, (d) 1000, (e) 1250, and (f) 1500 m. Positive (negative) values of Δt are represented by solid (dotted) contours. Although the vertical grid spacing is 125 m, every other level is omitted for brevity. Smoothed 20- and 40-dBZ reflectivity contours from the KLNX WSR-88D at the reference time are overlaid (thick black contours). The midlevel mesocyclone's location (orange star) is determined from 0.5° elevation WSR-88D velocity data that intersect the storm at ~2.5 km above radar level.

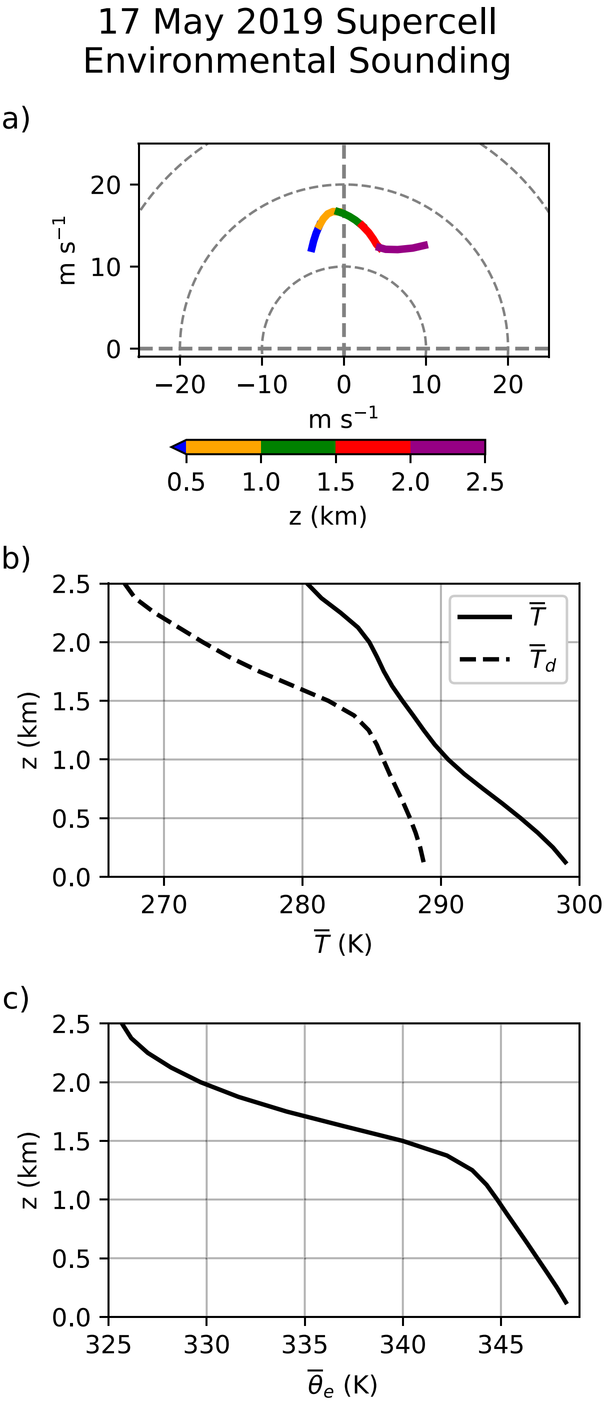

FIG. 4. The smoothed base-state (a) hodograph, (b) temperature ($\overline{T}$; solid black line) and dewpoint temperature ($\overline{T}_d$; dashed black line) profiles, and (c) $\overline{\theta}_e$ profile for the 17 May 2019 tornadic supercell environment. The sounding was derived by smoothing the vertical profiles of two of the earliest launched balloon-borne sondes at 2238 and 2248 UTC and then averaging the smoothed profiles.

TABLE 1. The $\overline{\theta}_e$ profiles (K) from smoothed base-state soundings for the 17, 20, and 23 May 2019 supercell cases.

z (m)	17 May	20 May	23 May
2500	325.7	342.3	332.2
2375	326.2	343.8	334.3
2250	327.0	345.1	336.6
2125	328.2	346.3	338.8
2000	329.7	347.3	340.7
1875	331.6	348.3	342.3
1750	334.1	349.2	343.6
1625	337.0	350.0	344.8
1500	340.0	350.8	345.8
1375	342.2	351.5	346.8
1250	343.5	352.1	347.7
1125	344.3	352.6	348.4
1000	344.8	353.2	349.1
875	345.3	353.9	349.6
750	345.8	354.5	350.2
625	346.4	355.2	350.7
500	346.9	355.8	351.1
375	347.4	356.2	351.5
250	347.9	356.6	351.9
125	348.3	356.9	352.1

κ_x = 1.4 km^2. However, given the aforementioned potential for horizontal, storm-relative position errors of several kilometers, an even more conservative κ_x was employed (i.e., greater smoothing), where κ_x = 44.2 km^2 for L_x = 5 km. A range of smoothing parameters was tested, and the degree of smoothing associated with L_x = 5 km was found to satisfactorily retain horizontal gradients without over-smoothing them.

Less smoothing was employed in the vertical. The vertical Barnes smoothing parameter, κ_z, was set to $\kappa_z = \kappa^* L_z^2 = 0.1\,\mathrm{km}^2$, where L_z = 0.25 km. The choice of L_z was based on an evaluation of the vertical data spacing and trial and error (i.e., this degree of smoothing retained vertical gradients without over-smoothing them).

A cutoff radius in the horizontal and vertical of $R = \sqrt{5\kappa_x}$ also was used in the interest of computational expediency (observations this far from a grid point have negligible weight). Last, after assigning values to all grid points, a spherical octant test was performed for each grid point to eliminate extrapolation beyond the observation region. Each octant of a sphere with radius R centered on the grid point was tested to see whether at least one observation was located within that octant, and only grid points with at least seven octants having at least one observation kept their assigned values (otherwise, the values were set to the null value).

To provide a means for assessing the degree to which the relatively long-duration time-to-space conversion might be adversely affecting the analyses, section 3 includes fields of Δt and the standard deviation of the Δts of the observations used to obtain each grid point value ($\sigma_{\Delta t}$). The Δt fields were objectively analyzed using the same Barnes analysis parameters that are used for the thermodynamic analyses. The $\sigma_{\Delta t}$ fields provide information about the reliability of patterns and gradients in the analyzed fields. For example, a small $\sigma_{\Delta t}$ (~5 min) at a particular grid point implies that the observations affecting that grid point's analysis value were at least obtained at approximately the same time, and a localized pattern evident in the

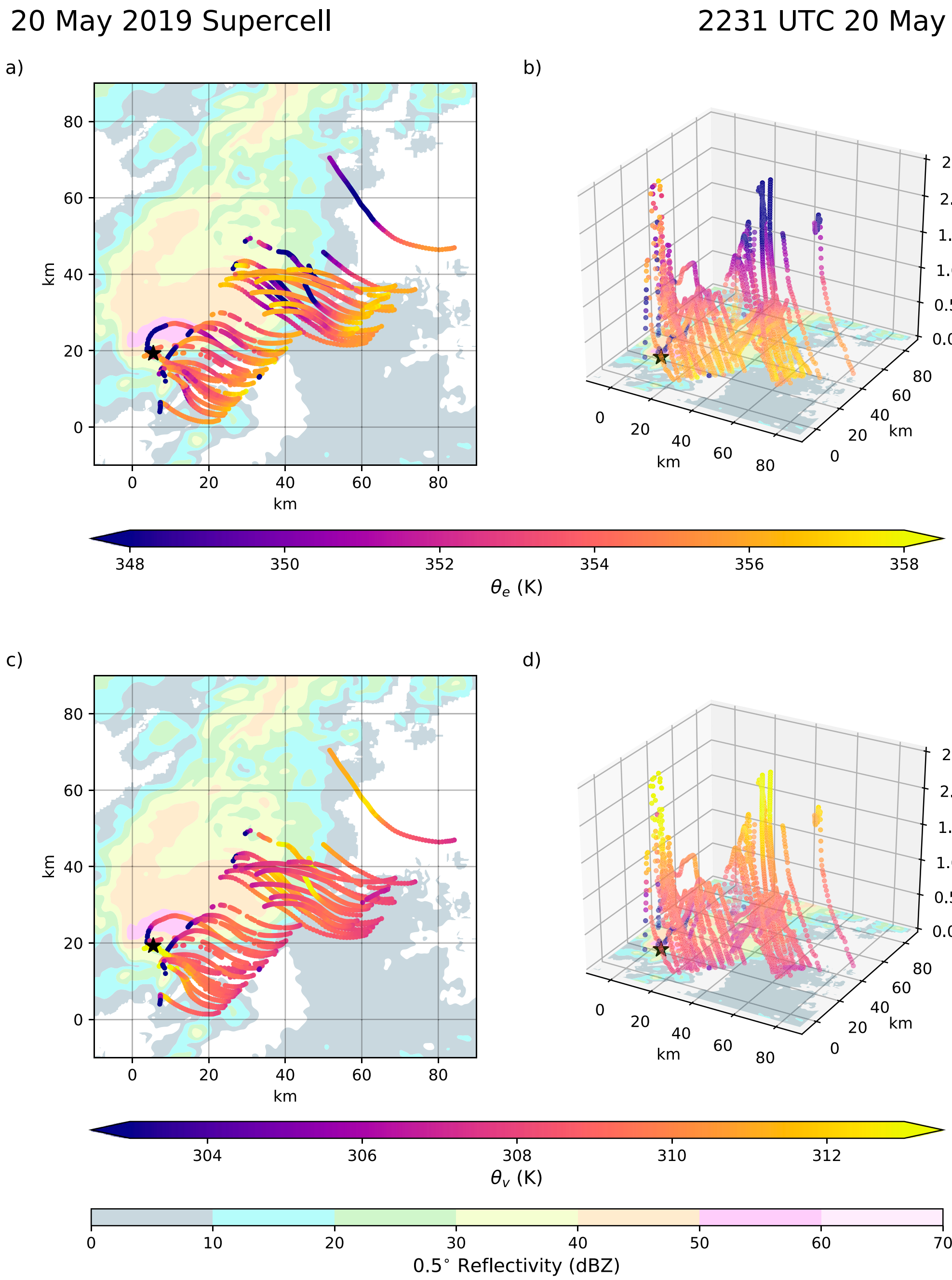

FIG. 5. As in Fig. 2, but for the 20 May 2019 tornadic supercell. The time-to-space conversion uses **c** = (11.8, 12.7) m s^{-1} and a reference time of 2231 UTC 20 May. The smoothed reflectivity field (lowest scan) is from the KFDR WSR-88D. The midlevel mesocyclone's location (black star) is determined from 0.5° elevation WSR-88D velocity data that intersect the storm at ~1.0 km above radar level.

analysis is not an artifact of observations being obtained over a long period of time during which substantial evolution occurred. On the other hand, the Δt fields provide information about the reliability of the correct storm-relative placement of patterns and gradients, with the placement error being $\Delta \mathbf{c} \Delta t$, where $\Delta \mathbf{c}$ is the storm motion "error" and represents a multitude of ways that the velocity of a storm feature can depart from the mean storm motion assumed in the time-to-space conversion, such as storm unsteadiness or simply the uncertainty in calculating a mean storm motion vector. However, our targeted observations are generally concentrated in the forward-flank region of the storm, where the thermodynamic fields do not typically evolve very rapidly. In an analysis of autocorrelations within the simulated

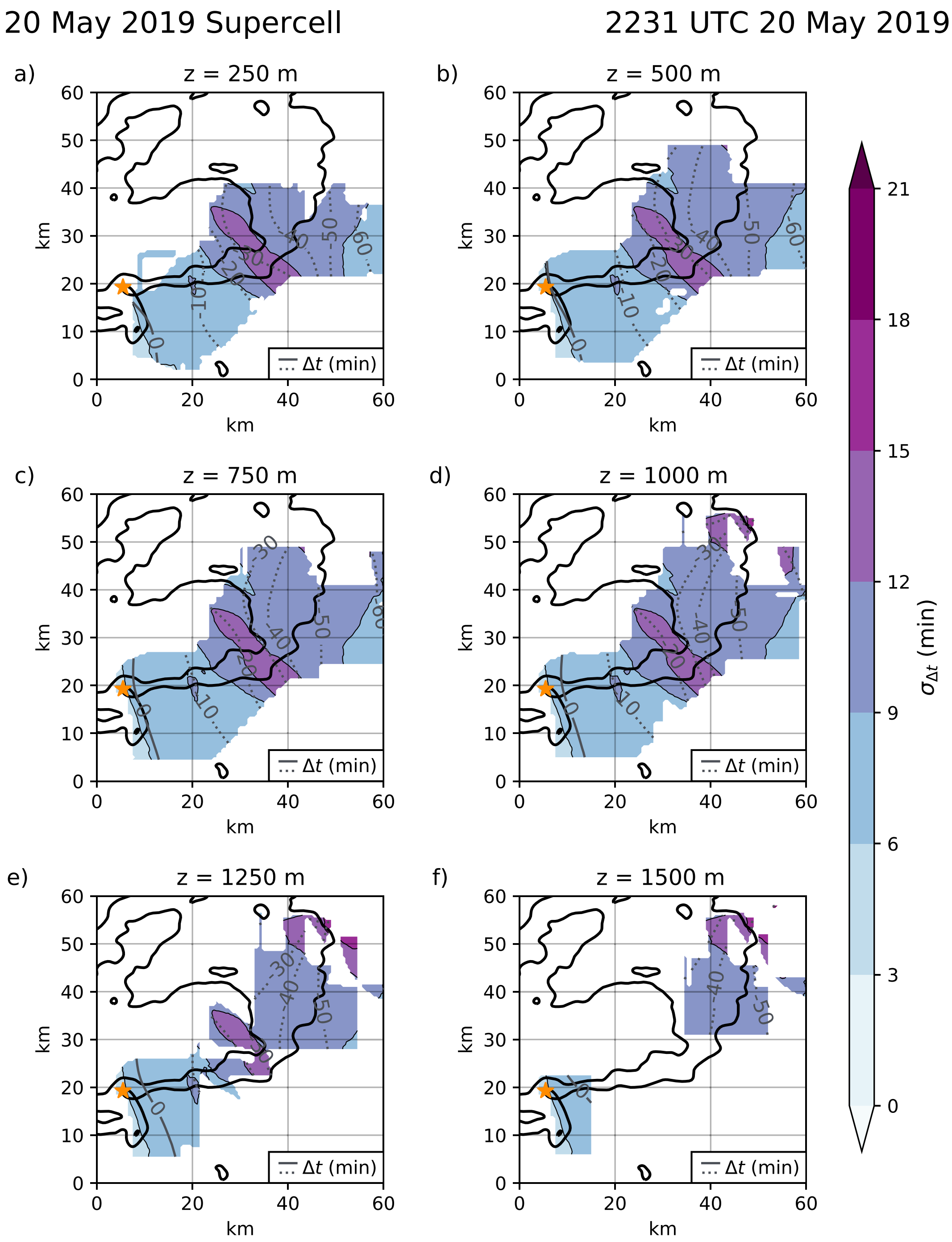

FIG. 6. As in Fig. 3, but for the 20 May 2019 supercell at the 2142 UTC 20 May reference time. Smoothed 20- and 40-dBZ reflectivity contours from the KFDR WSR-88D at the reference time are overlaid (thick black contours). The midlevel mesocyclone's location (orange star) is determined from 0.5° elevation WSR-88D velocity data that intersect the storm at ~1.0 km above radar level.

supercells of the Markowski (2020) study (not shown), it was found that the autocorrelation coefficient of the virtual potential temperature field in the forward flank remains at or above 0.9 for 10 min, and even after 30 min, remains ~0.7.

Some of the analyses presented in section 4 require the specification of a representative environment (i.e., a base-state) for the vertical profiles of equivalent potential temperature ($\overline{\theta}_e$) and virtual potential temperature ($\overline{\theta}_v$). The base-state profiles were determined either from the TORUS campaign's NSSL mobile upper-air soundings (Waugh 2020) or from some of our own balloon-borne sondes that ascended through the storm's inflow ahead of the precipitation. In either situation, the environmental profiles were obtained approximately 20 km from the targeted storms. Values of $\overline{\theta}_e$ and $\overline{\theta}_v$ were interpolated to each grid level via a one-dimensional Barnes scheme with the same κ_z used for the 3D analyses described above.

In section 4, the analyzed horizontal wind fields are used to estimate horizontal vorticity, and analyses of horizontal buoyancy gradients are used to make inferences about baroclinic horizontal vorticity generation. The horizontal vorticity $\boldsymbol{\omega}_h = \xi\,\mathbf{i} + \eta\,\mathbf{j}$ is estimated via

$$\boldsymbol{\omega}_h \approx -\frac{\partial v}{\partial z}\,\mathbf{i} + \frac{\partial u}{\partial z}\,\mathbf{j}, \tag{1}$$

which is valid where horizontal gradients in vertical velocity are small, such as in the forward-flank precipitation region of supercell storms where our targeted observations are typically most concentrated. The baroclinic horizontal vorticity generation is

$$\nabla \times B\mathbf{k} = \frac{\partial B}{\partial y}\,\mathbf{i} - \frac{\partial B}{\partial x}\,\mathbf{j}, \tag{2}$$

where the buoyancy B is approximated as $B \approx g(\theta'_v/\overline{\theta}_v)$, where g is the gravitational acceleration and θ'_v is the virtual potential temperature (θ_v) perturbation. (We use θ'_v rather than θ'_ρ, the density potential temperature, because we lack reliable observations of hydrometeor mass.) The baroclinic vorticity generation is related to the total change in the horizontal vorticity via

$$\frac{D\boldsymbol{\omega}_h}{Dt} = \boldsymbol{\omega}\cdot\nabla\mathbf{v}_h + \nabla \times B\mathbf{k}, \tag{3}$$

in the inviscid Boussinesq approximation. In section 4, the magnitude of baroclinic vorticity generated along a parcel's path toward a low-level mesocyclone is estimated from (3) via

$$\Delta|\boldsymbol{\omega}_h| \approx \frac{g}{\theta_{v0}}\overline{|\nabla_h\theta'_v|}\,\frac{\Delta s}{\overline{|\mathbf{v}_h|}}, \tag{4}$$

where g is the gravitational acceleration, θ_{v0} is the representative base-state θ_v, $\overline{|\nabla_h\theta'_v|}$ is the mean magnitude of the horizontal virtual potential temperature perturbation gradient averaged over Δs, Δs is the change in position along the parcel's path, and $\overline{|\mathbf{v}_h|}$ is the mean horizontal storm-relative wind speed. Mean refers to average quantities along the parcel's path in the 250–750-m layer.

Finally, all WSR-88D fields appearing in sections 3 and 4 have been smoothed via an isotropic two-dimensional Barnes objective analysis scheme. Reflectivity from the 0.5° elevation angle at the reference time for each case is smoothed in the horizontal direction with a $\kappa_x = \kappa^* L_x^2$, where $L_x = 0.75$ km. Admittedly, this is less smoothing than warranted by the radar data spacing in some cases (the distance to the nearest WSR-88D varies from case to case). However, given that the radar data are used only to help place the thermodynamic analyses in context (as opposed to being used to estimate hydrometeor mass, for example), it was deemed appropriate to use a fixed κ_x value for all cases that suppressed distracting small-scale features without over-smoothing key storm reflectivity

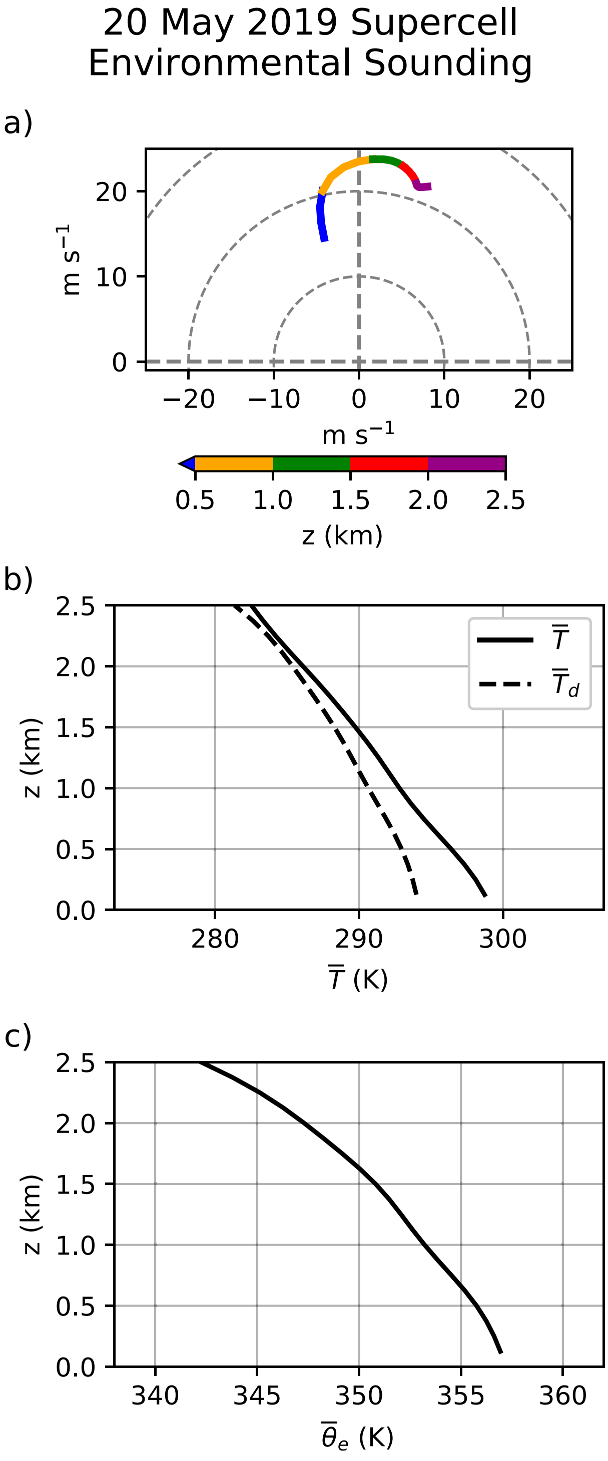

FIG. 7. As in Fig. 4, but for the 20 May 2019 tornadic supercell environment. The sounding was derived by smoothing the vertical profile of a NSSL mobile sounding launched at 2142 UTC 20 May.

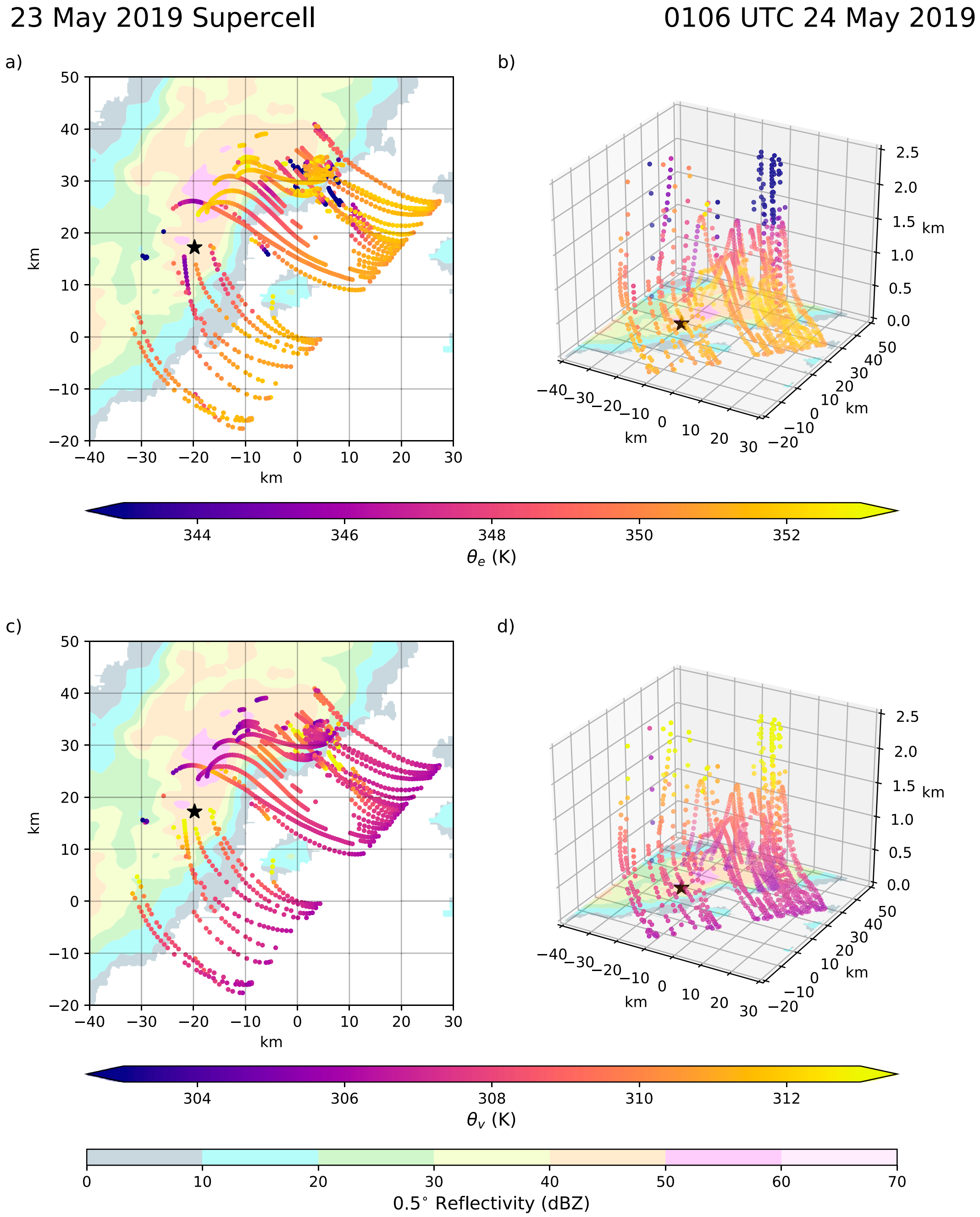

FIG. 8. As in Fig. 2, but for the 23 May 2019 tornadic supercell. The time-to-space conversion uses $\mathbf{c} = (8.5, 9.8)$ m s^{-1} and a reference time of 0106 UTC 24 May. The smoothed reflectivity field (lowest scan) is from the KDDC WSR-88D. The midlevel mesocyclone's location (black star) is determined from 0.5° elevation WSR-88D velocity data that intersect the storm at ~3.0 km above radar level.

structures (e.g., hook echo, forward-flank precipitation region). The horizontal grid spacing for the smoothed imagery is set to 250 m, and a cutoff radius of $\sqrt{5\kappa_x}$ is again used for computational expediency. To reduce extrapolation, a quadrant test with a four-quadrant threshold is performed, similar to the sonde data's octant test but only in the horizontal direction. Given the modest evolution of the radar reflectivity field over the duration of the data collection period, the smoothed reflectivity contours at the reference time should only be used as a general reference for inferring the storm-relative placement of gridded observations.

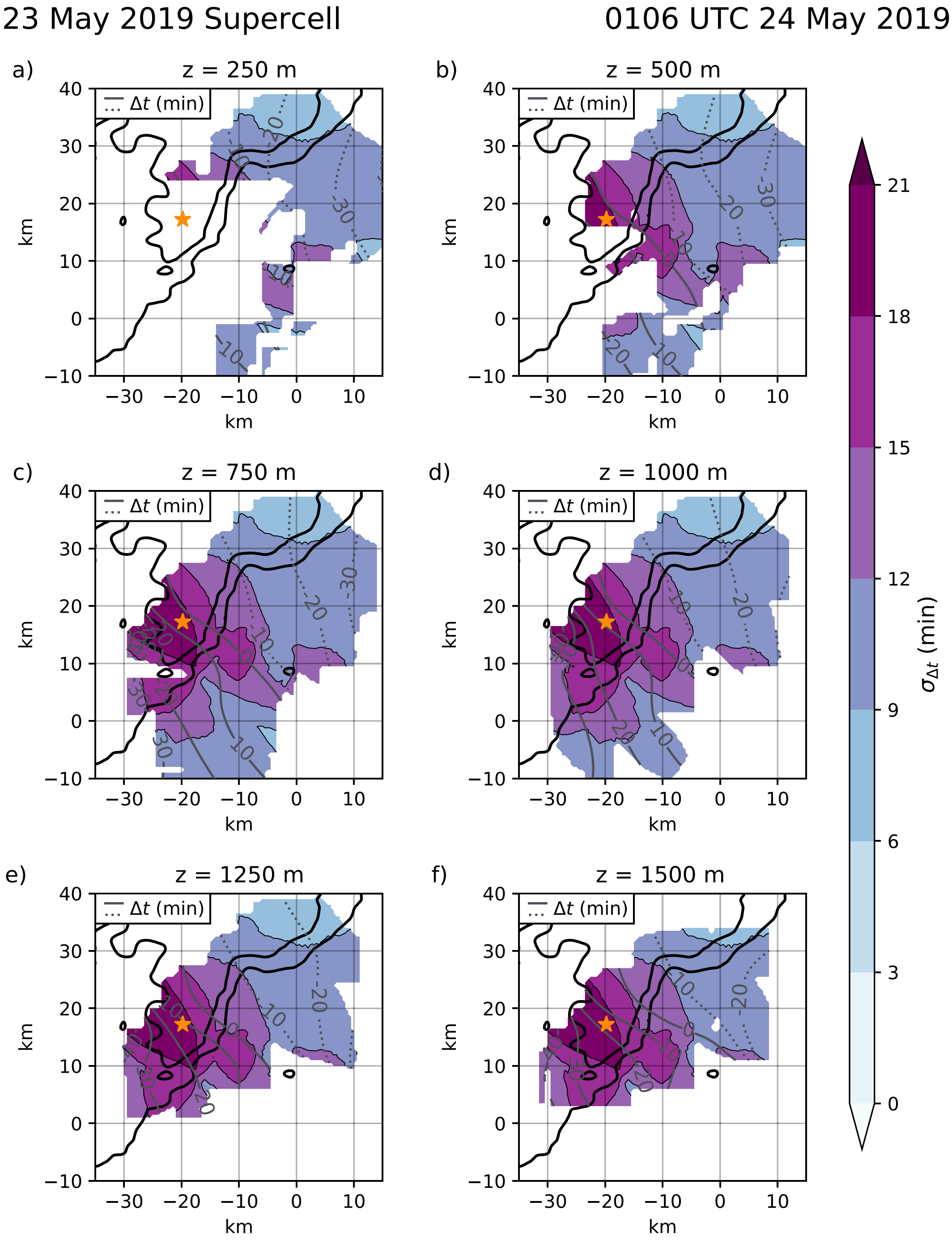

FIG. 9. As in Fig. 3, but for the 23 May 2019 supercell at the 0104 UTC 24 May reference time. Smoothed 20- and 40-dBZ reflectivity contours from the KDDC WSR-88D at the reference time are overlaid (thick black contours). The midlevel mesocyclone's location (orange star) is determined from 0.5° elevation WSR-88D velocity data that intersect the storm at ~1.0 km above radar level.

3. Case overviews

a. 17 May 2019, southwestern Nebraska

A tornadic supercell in southwestern Nebraska between McCook and Stockville was targeted in the afternoon and evening of 17 May 2019, with the two vans positioned to the east of Stockville (Fig. 1). During the deployment, the supercell spawned a 6-min EF2 tornado near McCook, a short-lived EF2 tornado northeast of Stockville, and five EF0 tornadoes throughout the data collection period (NOAA/NCEI 2021).

Thirty-three sondes entered the storm and collected data between 2229 UTC 17 May and 0002 UTC 18 May 2019 (Fig. 2). For the time-to-space conversion, $\mathbf{c} = (10.5, 11.7)$ m s^{-1} and a reference time of 0004 UTC 18 May 2019 were used. This reference time coincides with a 0.5° scan from the KLNX WSR-88D. Most of the sondes obtained observations within the forward-flank precipitation region; however, two sondes sampled areas closer to the updraft and hook area, with one sonde descending and passing through the hook echo before abruptly ascending again. Even though $|\Delta t|$ is as large as 60 min at the far northeast edge of the forward flank, $\sigma_{\Delta t}$ is typically 12 min or less throughout most of the storm (Fig. 3), which indicates that the local patterns and gradients in the analyses can be probably trusted. The environmental (base-state) profile (Fig. 4 and Table 1) was obtained by using an average of two of the earliest sondes, which were launched ~20 km northeast and upstream of the storm at 2238 and 2248 UTC 17 May 2019. Their storm-relative trajectories can be seen in Fig. 2 as the two highest-reaching sondes on the northeastern edge of the storm.

b. 20 May 2019, southwestern Oklahoma

In the afternoon of 20 May 2019, a tornadic supercell developed along the Oklahoma–Texas border and subsequently moved northeastward into southwestern Oklahoma, where it was intercepted. The supercell spawned brief EF0 tornadoes near Hollis, Gould, and Granite, as well as an EF2 tornado near Mangum during the deployment (NOAA/NCEI 2021). The two vans were first positioned south of Altus and then later repositioned farther north near Blair (Fig. 1), and the sondes collected data from 2055 to 2249 UTC 20 May. In total, 42 sondes entered the storm (Fig. 5). A reference time of 2231 UTC 20 May, coinciding with a 0.5° scan from the KFDR WSR-88D, and $\mathbf{c} = (11.8, 12.7)$ m s^{-1} were used for the time-to-space conversion. The sondes mostly passed through the southeastern portion of the forward-flank precipitation region and near/through the hook echo and updraft. Similar to the 17 May case, one of the sondes descended counterclockwise through the hook echo before ascending again. Observations influencing each grid point also occur at relatively similar times, as in the 17 May case, given that $\sigma_{\Delta t}$ is typically ~6–12 min throughout most of the storm, even though $|\Delta t|$ is as large as 60 min at the far eastern edge of the storm (Fig. 6). The environmental (base-state) conditions for this case were determined from a smoothed NSSL mobile sounding launched at 2142 UTC 20 May ~20 km southeast of the storm (Fig. 7 and Table 1).

c. 23 May 2019, northeastern Texas Panhandle

A tornadic supercell in the northeastern Texas Panhandle was targeted in the afternoon and evening of 23 May 2019. This storm produced an EF2 tornado near Canadian and later an EF3 tornado near Follett, Texas, and Laverne, Oklahoma, during the deployment period. The two vans, positioned near Higgins and south of Follett (Fig. 1), launched 48 sondes that sampled the storm from 0010 to 0210 UTC 24 May (Fig. 8). The sondes sampled the southwest forward-flank, mesocyclone, and rear-flank regions of the storm. The storm-relative sonde trajectories were determined using $\mathbf{c} = (8.5, 9.8)$ m s^{-1} and a reference time of 0106 UTC 24 May, which coincides with a 0.5° scan from the KDDC WSR-88D. Although $\sigma_{\Delta t}$ is typically ~10 min within the southern forward flank, $\sigma_{\Delta t}$ is as

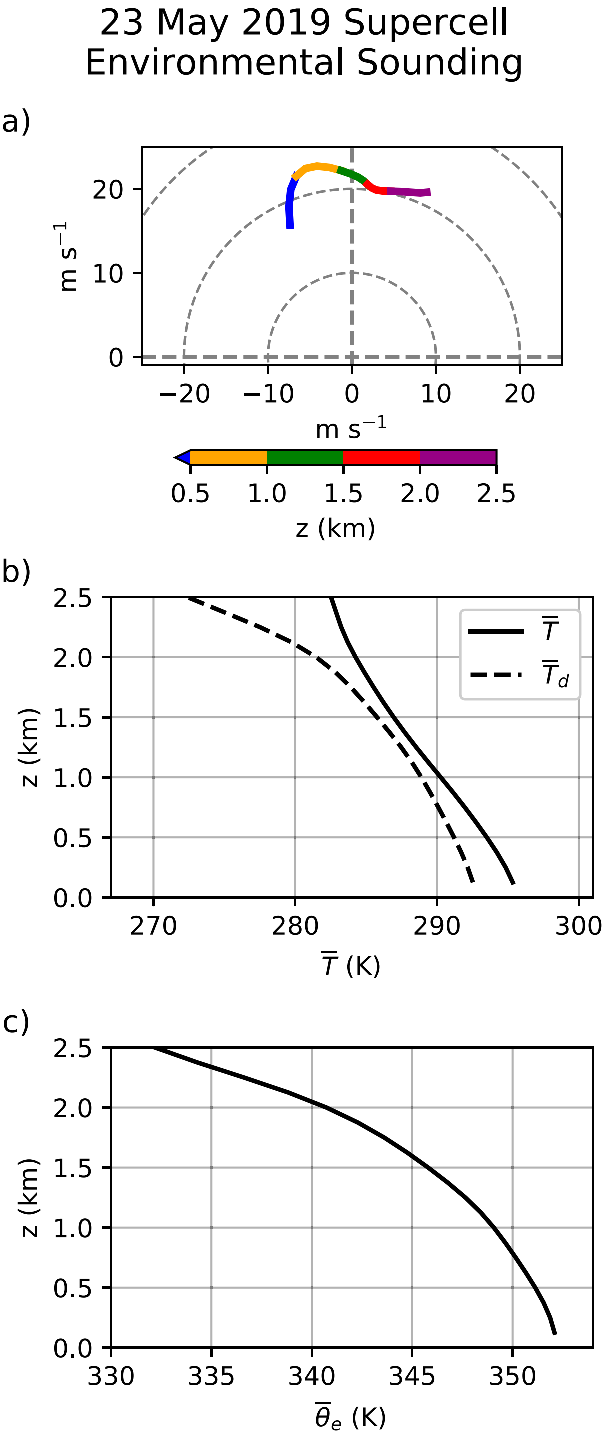

FIG. 10. As in Fig. 4, but for the 23 May 2019 tornadic supercell environment. The sounding was derived by smoothing the vertical profile of a NSSL mobile sounding launched at 0104 UTC 24 May.

large as 20 min within the southwestern forward flank, mesocyclone, and rear-flank areas (Fig. 9). However, $|\Delta t|$ is a bit smaller than in the other two cases, being ≤40 min. The environmental (base-state) conditions for this case were obtained from a NSSL mobile sounding launched ~20 km southeast of the storm at 0104 UTC 24 May 2019 (Fig. 10 and Table 1).

4. Results

Aboveground thermodynamic observations in these supercell thunderstorms can provide insight into vorticity generation processes and some aspects of flow structure. The baroclinic generation of vorticity in the cold pool is explored using θ'_v to derive horizontal buoyancy fields and associated horizontal baroclinic vorticity generation rate estimates. Comparing equivalent potential temperature (θ_e) observations to $\overline{\theta}_e$ gives a sense of inferred parcel origin height and, thus, the likely vertical excursions of parcels in different parts of the storm.

a. θ_e and inferred parcel origins

In all three supercells, θ_e generally decreases from northeast to southwest (i.e., from the forward flank toward the rear flank) within the portions of the outflow sampled by the sondes, at least in the lowest 1 km (Figs. 11–13; Figs. 14a,b–19a,b).[1] At the lowest levels sampled (e.g., $z \leq 500$ m), given the profiles of $\overline{\theta}_e$ (Figs. 4, 7, 10), the outflow of the 17 May, 20 May, and 23 May storms is characterized by θ_e deficits of up to 5, 9, and 4 K, respectively, with the largest deficits being observed on the rear flank, west of the mesocyclone locations. [In the 23 May storm, it seems likely that a pocket of lower-θ_e air was present in the lowest 500 m on the rear flank but was unsampled, given the low-θ_e air sampled in the region $z \geq 750$ m near $(x, y) = (-27, 15)$ km in Figs. 13c–f]. Deficits in θ_e generally decrease with height in all three storms.

The maximum θ_e deficits analyzed at the lowest grid levels in all three storms compare well with the maximum θ_e deficits in tornadic supercells reported by Shabbott and Markowski (2006) in their survey of mobile mesonet observations within supercell forward-flank outflow. They found, on average, maximum θ_e deficits of 6.4 and 11.2 K, respectively, in the tornadic and nontornadic supercells in their dataset, though some caution is warranted in comparing mobile mesonet observations obtained at $z = 2$ m to the thermodynamic analyses herein, even at the lowest grid levels. Also in agreement with previous studies, the strong, approximately eastward-pointing θ_e gradient (i.e., tightly packed and roughly north–south-oriented θ_e contours) sampled north of the mesocyclones of all three supercells between their forward and rear flanks, resembles the "left-flank convergence boundary" identified in the numerical simulation of Beck and Weiss (2013) (Figs. 11b, 12a–c, and 13b,c).

Altitudes from which outflow air parcels originate in the environment (z_{orig}) were inferred from the θ_e analyses and vertical profiles of $\overline{\theta}_e$ assuming that parcels conserved their θ_e (Figs. 14a,b–19a,b; Figs. 20–22).[2] Although mixing, and to a very small extent phase changes, can lead to non-conservation of θ_e along trajectories, the fields of z_{orig} are still useful for qualitatively assessing the vertical excursions ($z - z_{\mathrm{orig}}$) of air parcels. In general, the θ_e fields within the forward-flank precipitation regions of all three storms, where θ_e deficits are only a few degrees, suggest only small downward vertical excursions, generally ≤200 m. That is, air parcels rained into as they pass through the forward-flank precipitation region en route to the mesocyclone or rear flank of the storm only descend very gradually during their journey through the forward flank. This finding is consistent with trajectories computed from dual-Doppler observations [e.g., Fig. 14 in Klemp et al. (1981); Fig. 14a in Kosiba et al. (2013)] and numerical simulations [e.g., Fig. 12d in Klemp et al. (1981); Fig. 6 in Dahl (2015)] of supercells.

On the other hand, on the rear flank of the storm, including the hook echo and mesocyclone regions, where the aforementioned larger θ_e deficits (and also stronger horizontal θ_e gradients) are found, much larger downward vertical excursions (and large horizontal gradients in z_{orig}) are inferred (Figs. 15a,b, 17a,b, 19a,b, and 20–22). For instance, in the 20 May supercell (Figs. 17a,b and 21), parcels on the rear flank below ≲500 m are associated with $z_{\mathrm{orig}} \sim$ 1000–2000 m. In the 23 May supercell (Figs. 19a,b and 22), air from above 2 km is inferred to have penetrated down to at least 750 m (and perhaps to the surface, though the lower levels on the rear flank were not sampled by any sondes, unfortunately).

The sondes also sampled regions in which net upward displacements of air could be inferred from the θ_e and z_{orig} fields (where $\theta'_e > 0$ and $z - z_{\mathrm{orig}} > 0$), presumably within updraft regions (as explained in section 2, the vertical velocity of the air is unknown because the accumulated water mass and fall speeds of the sondes are unknown). For example, a plume of upward displacements is evident in the 17, 20, and 23 May analyses on the western (left) side (i.e., near/within the mesocyclone) of the vertical cross sections shown in Figs. 15a,b, 17a,b, and 19a,b, respectively. These plumes can be also seen near the midlevel mesocyclone at 1250–1500 m in the z_{orig} field (Figs. 20e,f; 21e,f; and 22e,f).

b. Buoyancy, $\boldsymbol{\omega}_h$, and baroclinic vorticity generation

In the 17 May supercell, θ_v deficits over 5 K are present at the lowest grid levels within the outflow 5–10 km north of the mesocyclone (Figs. 23a,b). This θ'_v minimum in the outflow is on the cooler end of the spectrum of the tornadic supercell outflows in the Shabbott and Markowski (2006) study. In the 20 May and 23 May supercells, the cold pool sampled by the sondes is considerably weaker at the lowest grid levels, with

---

[1] In Figs. 14–19, two vertical cross sections are drawn for each supercell to highlight differences between the forward flank and rear flank of the storm. For each case, cross section AB intersects the forward flank, whereas cross section CD intersects the mesocyclone and rear-flank areas. The orientation of all cross sections were chosen to be nearly along the thermodynamic gradients.

[2] To obtain z_{orig} for each case, θ_e was matched to heights in the $\overline{\theta}_e$ profile via linear interpolation.

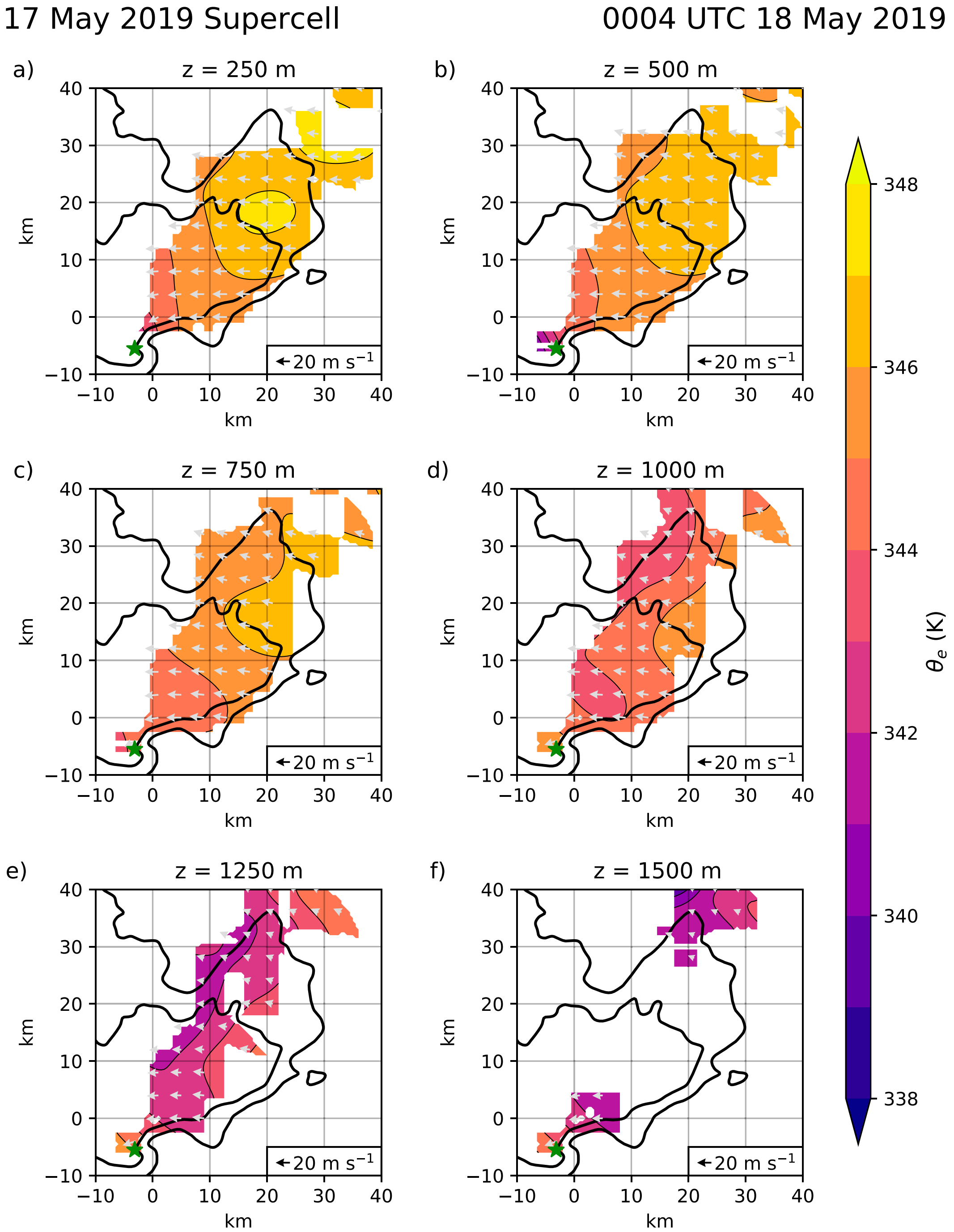

FIG. 11. Horizontal cross sections of θ_e (shading; K) and storm-relative winds (vectors; m s^{-1}) in the 17 May 2019 supercell at (a) 250, (b) 500, (c) 750, (d) 1000, (e) 1250, and (f) 1500 m. Although the vertical grid spacing is 125 m, every other level is omitted for brevity. Wind vectors are plotted every 4 km, and the smoothed 20- and 40-dBZ reflectivity contours from the KLNX WSR-88D at the reference time (0004 UTC 18 May) are also overlaid (thick black contours). The midlevel mesocyclone's location (green star) is determined from 0.5° elevation WSR-88D velocity data that intersect the storm at ~2.5 km above radar level.

maximum θ_v deficits of only 2–4 K (Figs. 24a–c and 25a–c), which is more typical of the outflow strength found in prior studies to be associated with tornadic supercells (Markowski et al. 2002; Shabbott and Markowski 2006; Grzych et al. 2007; Hirth et al. 2008; Weiss et al. 2015). However, the portions of the outflow likely to be the coldest (e.g., the region 5–10 km north and west of the mesocyclone) were not as well sampled in either of the 20 or 23 May supercells, as in the 17 May case.

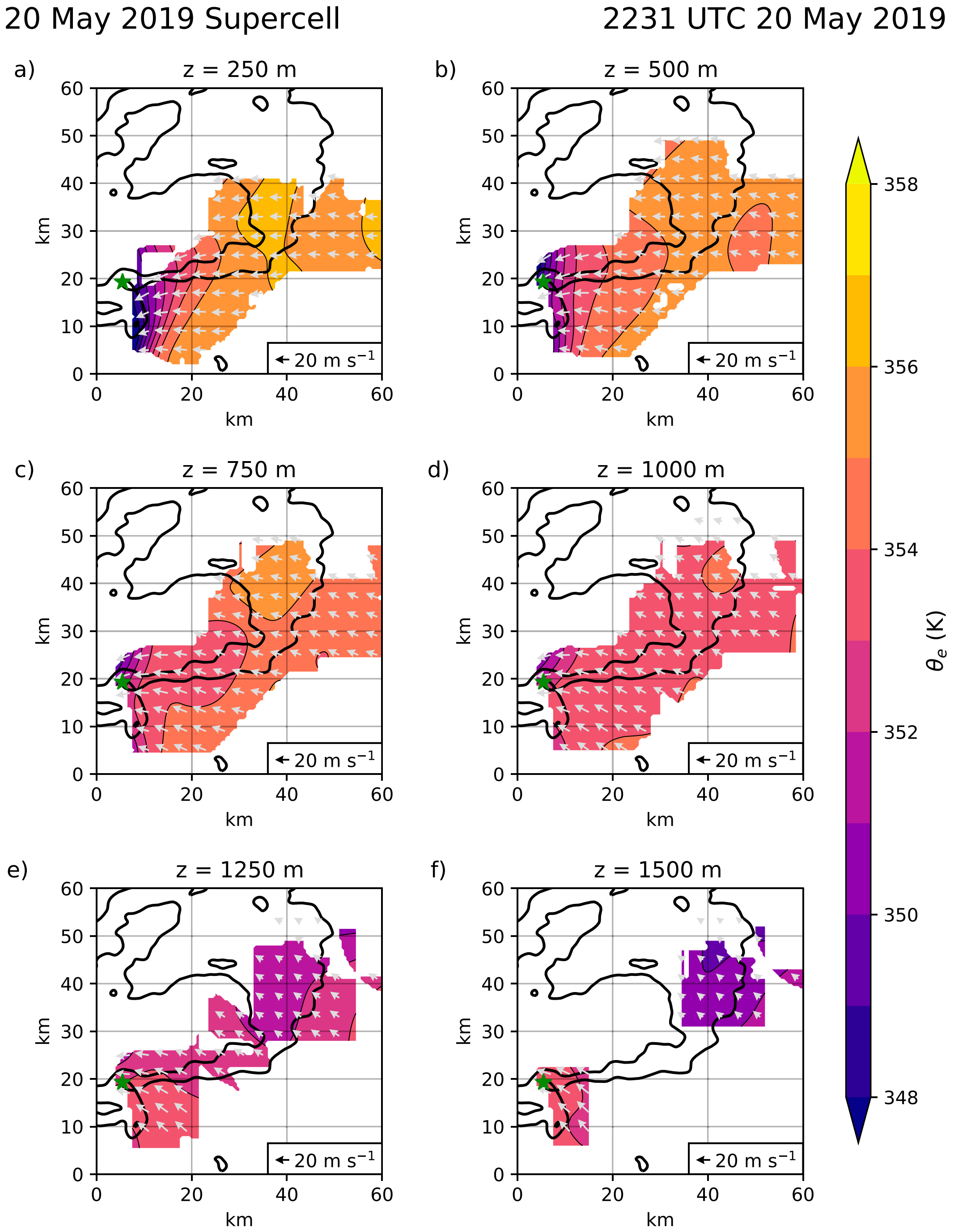

FIG. 12. As in Fig. 11, but for the 20 May 2019 supercell. The smoothed 20- and 40-dB*Z* reflectivity contours (thick black contours) are from the KFDR WSR-88D at the reference time (2142 UTC 20 May). The midlevel mesocyclone's location (green star) is determined from 0.5° elevation WSR-88D velocity data that intersect the storm at ~1.0 km above radar level.

It also can be noted that in all three storms, the strongest θ_v deficit areas at lower levels just to the west/southwest of the mesocyclone (where the hook and rear flank would be) coincide with higher z_{orig} and lower θ_e values (i.e., larger vertical descent; cf. Figs. 15c,d; 17c,d; 19c,d to Figs. 15a,b; 17a,b; 19a,b), which may be evidence of greater evaporational cooling and/or melting in the rear-flank downdraft.

One outstanding question over the years concerns the depth of supercell cold pools and associated baroclinity (horizontal θ_v gradients) along trajectories that approach the low-

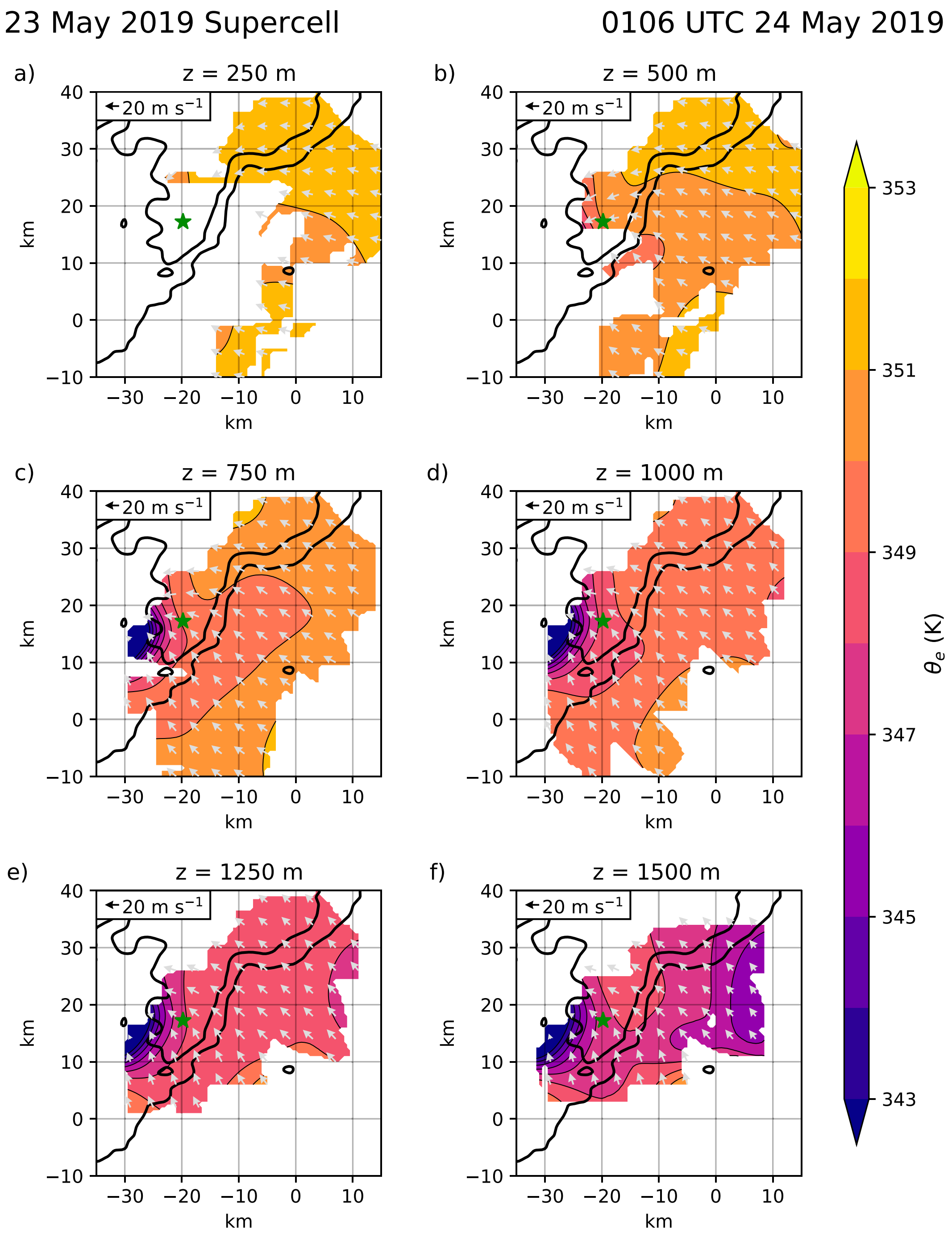

FIG. 13. As in Fig. 11, but for the 23 May 2019 supercell. The smoothed 20- and 40-dBZ reflectivity contours (thick black contours) are from the KDDC WSR-88D at the reference time (0004 UTC 18 May). The midlevel mesocyclone's location (green star) is determined from 0.5° elevation WSR-88D velocity data that intersect the storm at ~3.0 km above radar level.

level mesocyclone or tornado. In all three storms, the largest θ_v deficits are at the lowest grid level. In the 17 May storm, θ_v' increases approximately linearly with height up to the top of the data region (z = 1.25–1.5 km), where θ_v deficits of 1–2 K remain (Figs. 14c,d, 15c,d, and 26). The most significant baroclinity resides in the lowest 750 m, with the magnitude of the vorticity generation rate $\gtrsim 1.0 \times 10^{-5}$ s^{-2} at 250 m (Fig. 23). In the May 20 storm, θ_v deficits of 1–2 K also remain at the top of the data region at ~1.25 km (Figs. 17c,d and 27) and the baroclinity, which is weaker than in the 17 May

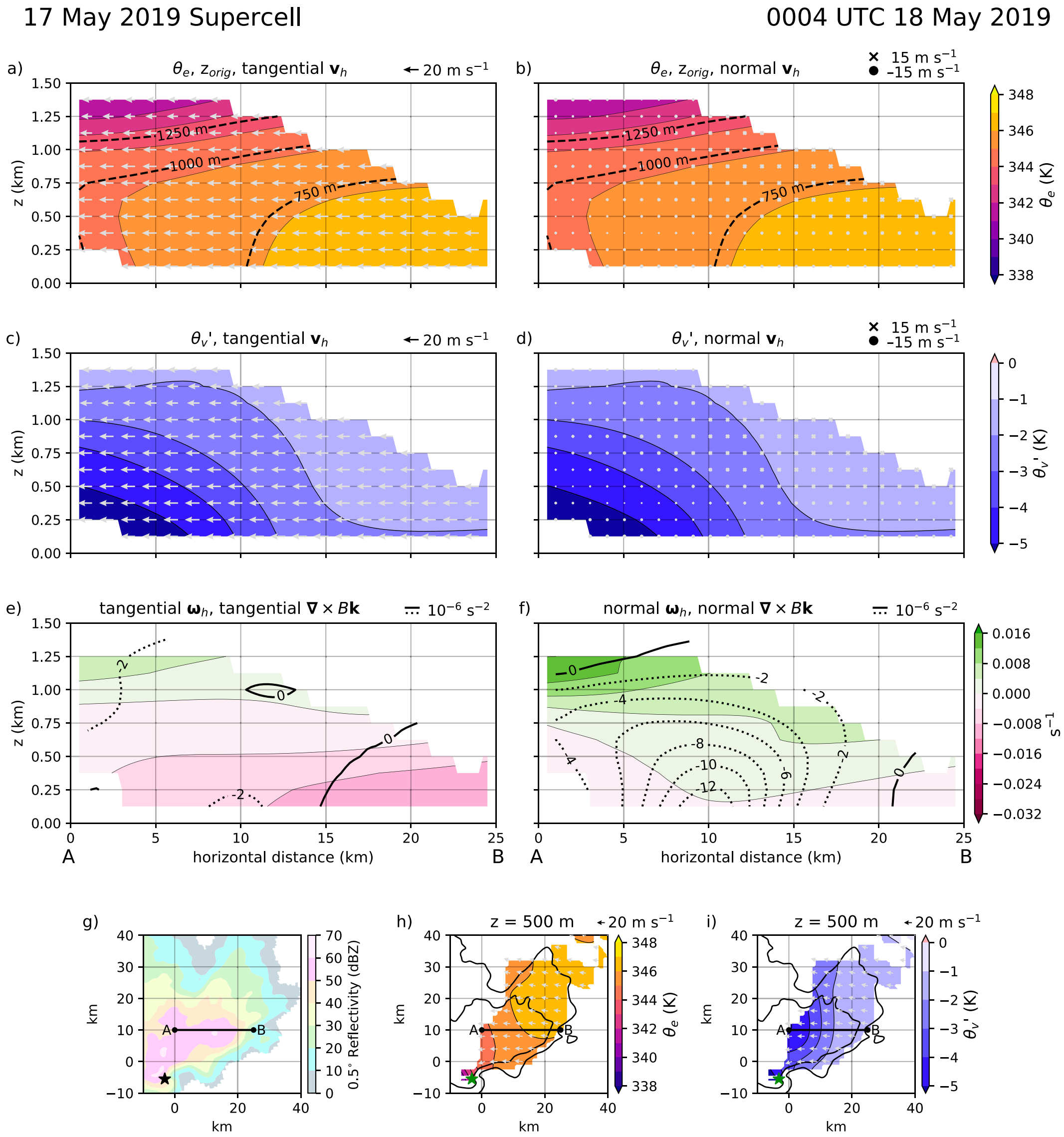

FIG. 14. Vertical cross section AB for the 17 May 2019 supercell, oriented from west to east in the forward-flank precipitation region. (a) θ_e (shading; K) and z_{orig} (black dashed contours; m) with tangential storm-relative winds (m s^{-1}), (b) θ_e (shading; K) and z_{orig} (black dashed contours; m) with normal storm-relative winds (m s^{-1}), (c) θ_v' (shading; K) with tangential storm-relative winds (m s^{-1}), (d) θ_v' (shading; K) with normal storm-relative winds (m s^{-1}), (e) tangential horizontal vorticity ($\boldsymbol{\omega}_h$; shading; s^{-1}) with tangential baroclinic vorticity generation rate ($\nabla \times B\mathbf{k}$; black contours; 10^{-6} s^{-2}), and (f) normal horizontal vorticity ($\boldsymbol{\omega}_h$; shading; s^{-1}) with normal baroclinic vorticity generation rate ($\nabla \times B\mathbf{k}$; black contours; 10^{-6} s^{-2}). The wind vectors in (a) and (c) are plotted at every fifth grid point and every 125 m in the horizontal and vertical directions, respectively, and the wind symbols in (b) and (d) are plotted every fourth grid point and every 125 m in the horizontal and vertical directions, respectively. Normal wind components into (out of) the cross section in (b) and (d) are positive (negative) and are indicated by × (●). In (e), tangential components to the right (left) along the cross section are positive (negative), and in (f) normal components into (out of) the cross section are positive (negative). For baroclinic vorticity generation rate, positive (negative) contours are solid (dashed). For reference, the cross-section position in the horizontal plane is shown atop (g) smoothed radar reflectivity imagery from the KLNX WSR-88D at the reference time (0004 UTC 18 May), (h) the θ_e and storm-relative wind fields at $z = 500$ m, and (i) the θ_v' and storm-relative wind fields at $z = 500$ m. The smoothed 20- and 40-dBZ reflectivity contours at this time are also plotted as thick black lines in (h) and (i), and the location of the midlevel mesocyclone is indicated by a black star in (g) and green star in (h) and (i). The mesocyclone's location is determined from 0.5° elevation WSR-88D velocity data that intersect the storm at ~2.5 km above radar level.

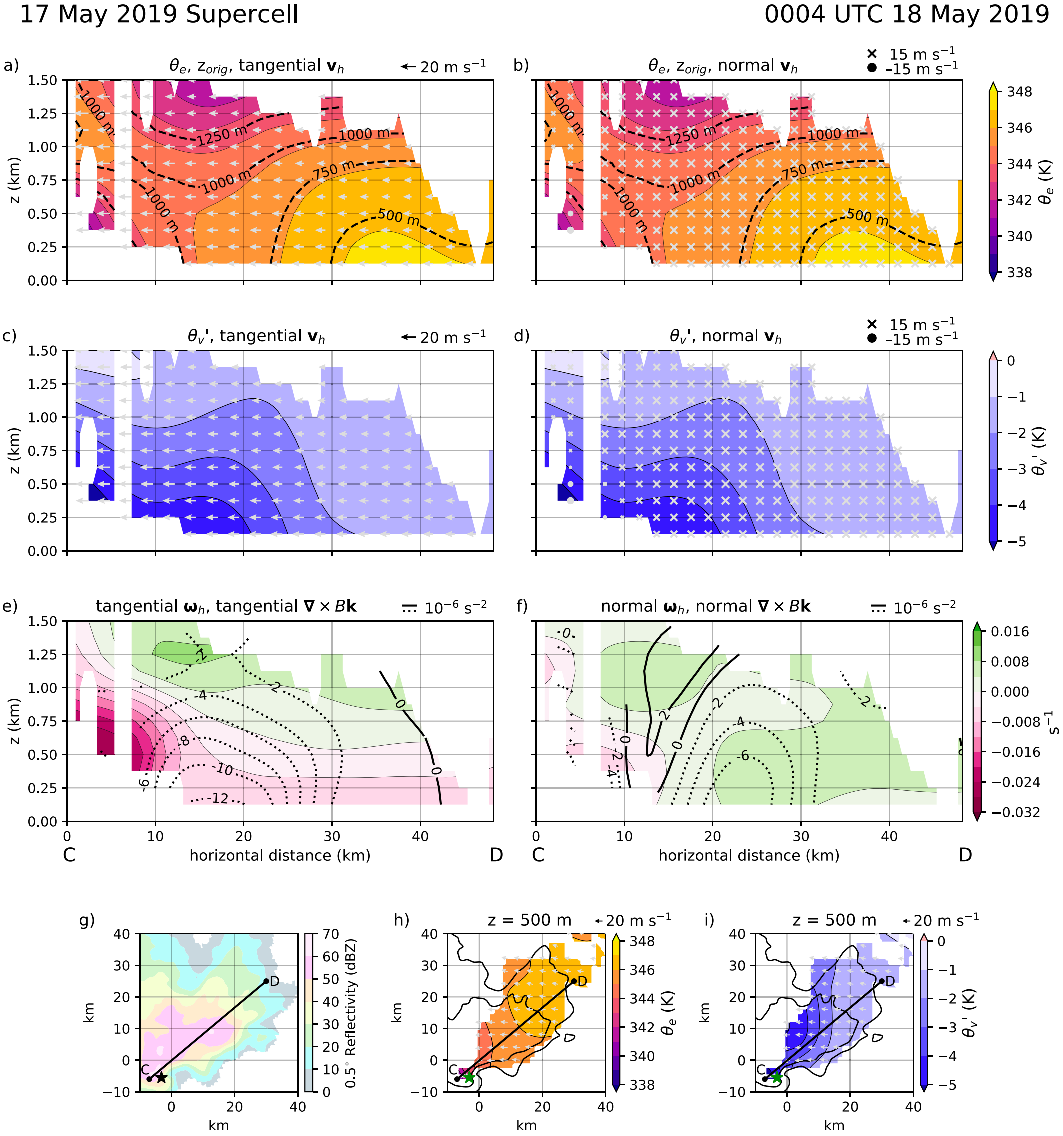

FIG. 15. As in Fig. 14, but for vertical cross section CD through the 17 May 2019 supercell. The cross section extends from the hook echo in the southwest to the edge of the forward-flank precipitation region in the northeast. Reflectivity imagery from the KLNX WSR-88D at the reference time (0004 UTC 17 May) is shown in (g)–(i), and the location of the midlevel mesocyclone is indicated by a black star in (g) and green star in (h) and (i). The mesocyclone's location is determined from 0.5° elevation WSR-88D velocity data that intersect the storm at ~2.5 km above radar level.

storm (θ_v deficits are smaller, as noted above), is also most significant in the lowest 750 m (Figs. 17c,d and 24). The 23 May storm has the weakest baroclinity, at least in the forward-flank precipitation region, where the depth of the outflow is not well-defined given the small θ_v deficits (Figs. 18c,d, 25, and 28). A stronger, deeper cold pool was sampled 5–10 km west of the mesocyclone in the rear-flank region (Figs. 19c,d, 25, and 28). Trajectories bound for the low-level mesocyclone are unlikely to have passed through this baroclinity given its location so far west.

The direction of the baroclinic vorticity generation lies along the θ'_v contours (neglecting the effects of hydrometeors on buoyancy) with cold air on the right. In general, the baroclinic vorticity generation experienced by the air parcels that approach the storms from the east, enter the forward-flank precipitation region, descend gradually and eventually turn southward to enter the low-level mesocyclone from the north or northeast [as in the simulations of Rotunno and Klemp (1985), Adlerman et al. (1999), Markowski and Richardson (2014), and Dahl (2015), or the dual-Doppler-derived

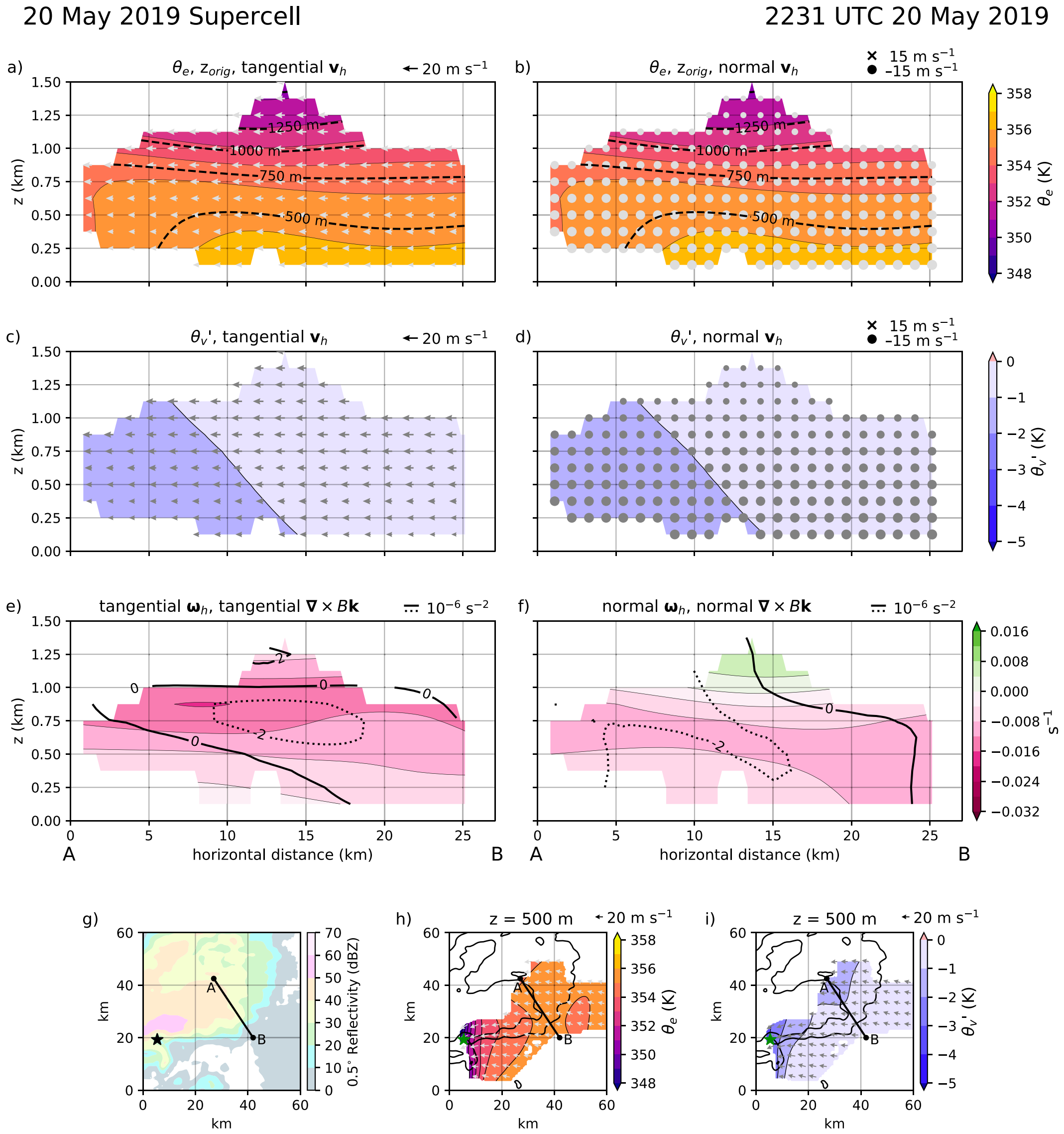

FIG. 16. As in Fig. 14, but for vertical cross section AB through the 20 May 2019 supercell. The cross section extends from northwest to southeast in the forward-flank precipitation region. Reflectivity imagery from the KFDR WSR-88D at the reference time (2231 UTC 20 May) is shown in (g)–(i), and the location of the midlevel mesocyclone is indicated by a black star in (g) and green star in (h) and (i). The mesocyclone's location is determined from 0.5° elevation WSR-88D velocity data that intersect the storm at ~1.0 km above radar level.

trajectories of Klemp et al. (1981), Brandes (1984b), and Kosiba et al. (2013)] would have a substantial crosswise component. For example, in the 17 May storm, the generation is directed mainly to the south and southwest within the forward-flank precipitation in the lowest 750 m (Figs. 14c–f, 15c–f, and 23c,f,i), where the storm-relative winds are predominantly easterly. The 20 May (Figs. 16c–f, 17c–f, and 24c,f,i) and 23 May (Fig. 25c,f,i) storms are similar in this regard.

The amount of baroclinic vorticity generated along a parcel's path toward a low-level mesocyclone can be estimated via (4). The vorticity generation is estimated for each case along trajectories (refer to the orange arrows in Figs. 23a, 24a, and 25a) that are optimally positioned in the lowest 750 m to exploit the entire length of the storm's most favorable region for baroclinic generation (at least the most favorable given the limitations of the data). In the lowest 750 m of the 17 May supercell (Fig. 23), given a θ_{v0} of 312 K, Δs of ~25 km, $\overline{|\mathbf{v}_h|}$ of ~20 m s^{-1}, and $\overline{|\nabla_h \theta_v'|} \approx 2.5 \times 10^{-4}$ K m^{-1}, ≈0.01 s^{-1} baroclinic vorticity would be generated along a parcel's path by the time it reaches the low-level mesocyclone. In the 20 May supercell's lowest 750 m (Fig. 24), ≈0.006 s^{-1} baroclinic vorticity

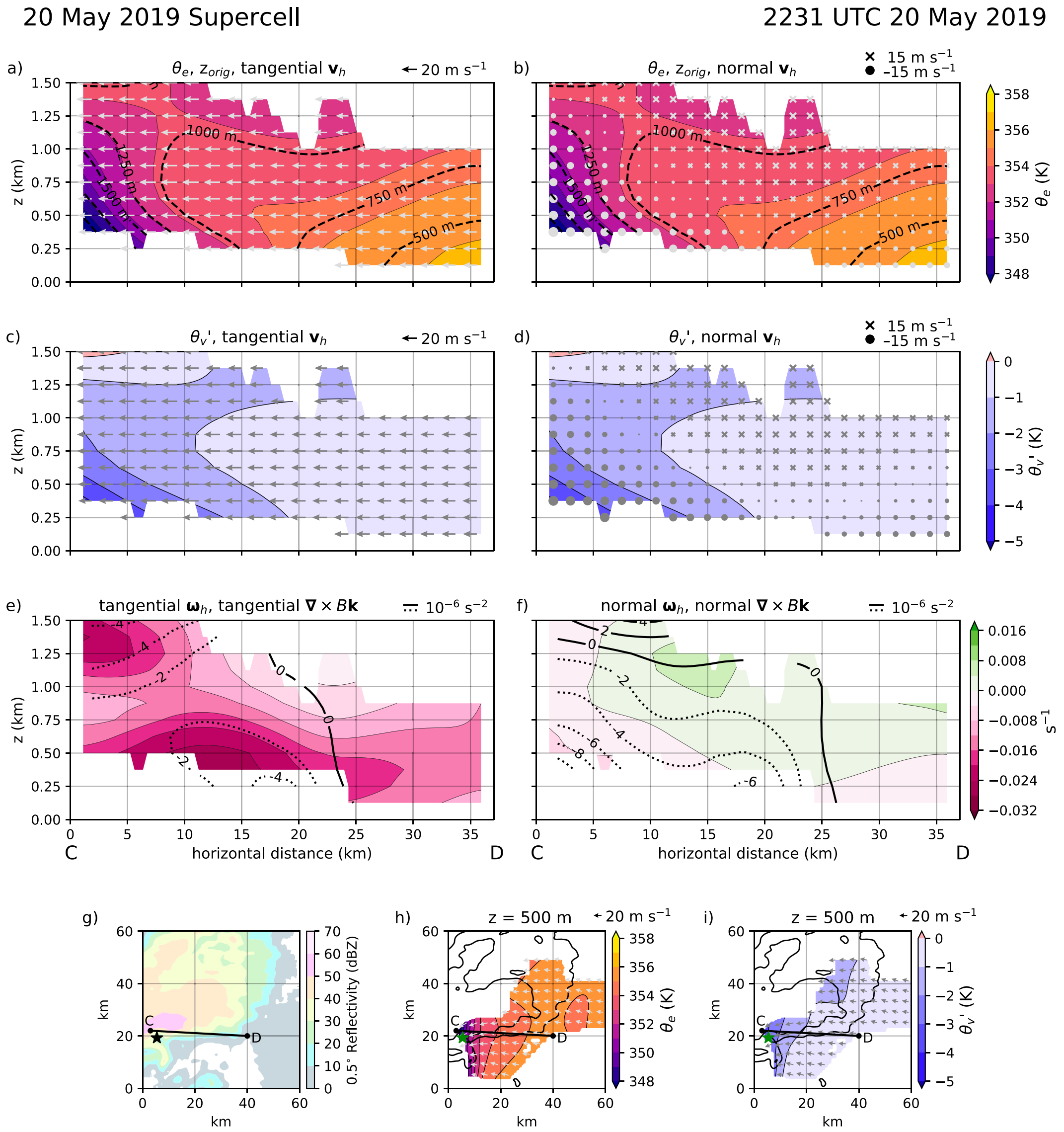

FIG. 17. As in Fig. 14, but for vertical cross section CD through the 20 May 2019 supercell. The cross section extends from west to east from the western edge of the mesocyclone to the southeastern edge of the forward-flank precipitation. Reflectivity imagery from the KFDR WSR-88D at the reference time (2231 UTC 20 May) is shown in (g)–(i), and the location of the midlevel mesocyclone is indicated by a black star in (g) and green star in (h) and (i). The mesocyclone's location is determined from 0.5° elevation WSR-88D velocity data that intersect the storm at ~1.0 km above radar level.

would be generated along a parcel's path to the mesocyclone, given a θ_{v0} of 309 K, Δs of ~45 km, $\overline{|\mathbf{v}_h|}$ of ~18 m s^{-1}, and $\overline{|\nabla_h \theta_v'|} \approx 7.5 \times 10^{-5}$ K m^{-1}. Parcels in these two supercells may, thus, gain nontrivial baroclinic vorticity to enhance the total $\boldsymbol{\omega}_h$. Along a parcel's path in the 23 May supercell's lowest 750 m (Fig. 25), only ≈0.003 s^{-1} baroclinic vorticity would be generated, given a θ_{v0} of 309 K, Δs of ~30 km, $\overline{|\mathbf{v}_h|}$ of ~15 m s^{-1}, and $\overline{|\nabla_h \theta_v'|} \approx 4.0 \times 10^{-5}$ K m^{-1}. Unfortunately, the limited sampling of the forward-flank baroclinic zone (only the southwestern portion of the forward flank was observed) prevents a more accurate estimate of the baroclinic vorticity generation for this case. However, the baroclinic vorticity generation estimates in all three cases may be underestimated owing to excessive smoothing[3] and by not including hydrometeor mass. Hydrometeor mass increases the

---

[3] The baroclinic generation of low-level, *mesocyclone-scale circulation* might not be underestimated by smoothing. The generation of such circulation is more a function of the buoyancy differential across the broad envelope of trajectories feeding the low-level mesocyclone than on the fickle maximum horizontal gradient somewhere within that envelope [Davies-Jones 2015, see his Eqs. (5) and (6)]. The horizontal buoyancy differential across a broad baroclinic zone would be less sensitive to smoothing than a localized horizontal buoyancy gradient. However, the exclusion of hydrometeor effects might be expected to lead to underestimates of baroclinic circulation generation as it does for baroclinic vorticity generation.

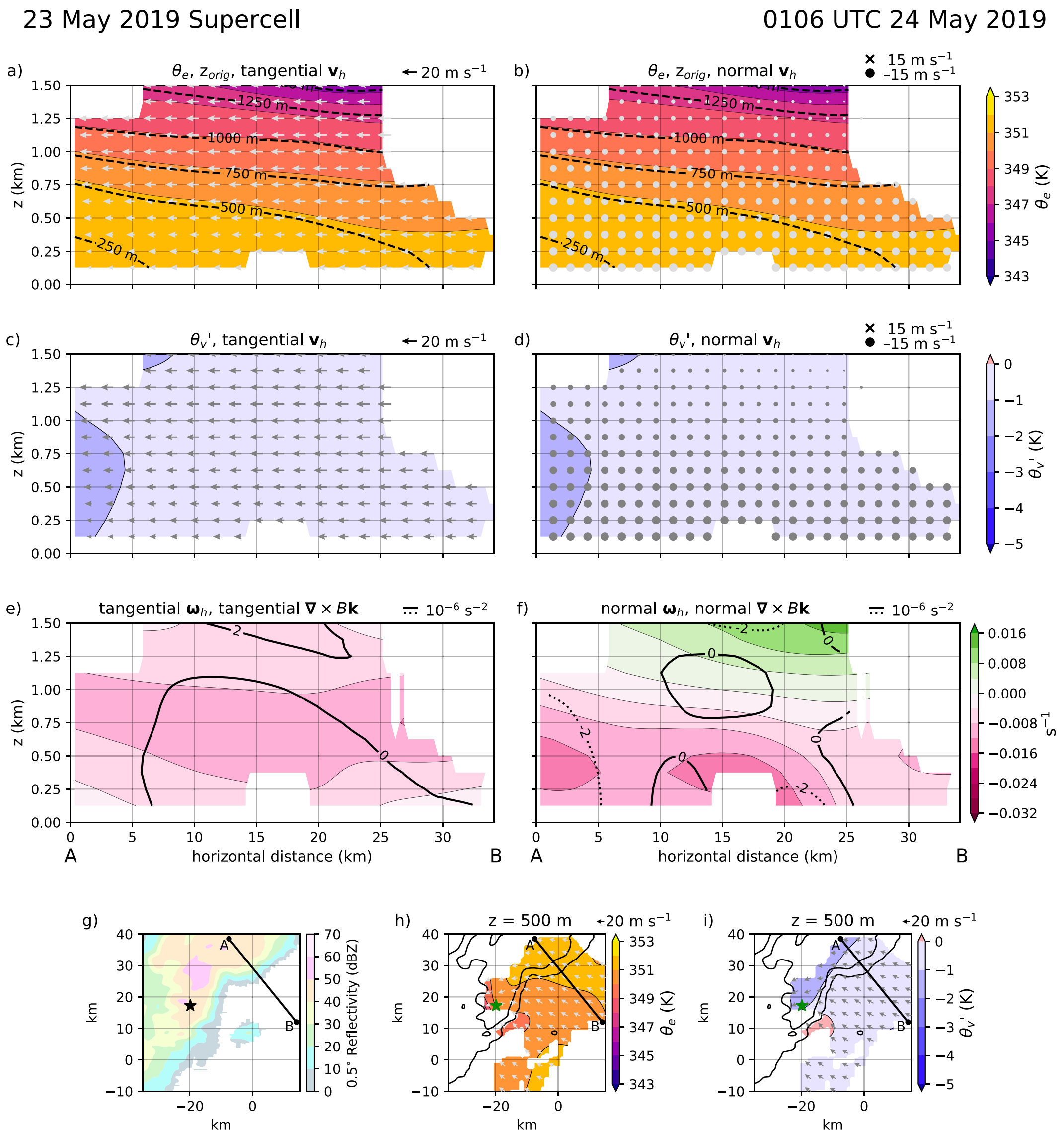

FIG. 18. As in Fig. 14, but for vertical cross section AB through the 23 May 2019 supercell. The cross section extends from northwest to southeast from the forward-flank precipitation into the environment. Reflectivity imagery from the KDDC WSR-88D at the reference time (0106 UTC 24 May) is shown in (g)–(i), and the location of the midlevel mesocyclone is indicated by a black star in (g) and green star in (h) and (i). The mesocyclone's location is determined from 0.5° elevation WSR-88D velocity data that intersect the storm at ~3.0 km above radar level.

negative buoyancy of the outflow, thereby enhancing the horizontal buoyancy differential from the outflow to the environment, along with the average baroclinic vorticity generation rate. In all three storms, comparing estimated $\Delta\boldsymbol{\omega}_h$ via (4) to the changes in gridded $\boldsymbol{\omega}_h$ from along the trajectories is ill-advised because of challenges in computing other terms in the vorticity budget and the fact that the gridded $\boldsymbol{\omega}_h$ fields neglect horizontal gradients of vertical velocity.

We cannot say for certain what subsequently happens to the baroclinically generated horizontal vorticity for parcels that eventually enter the mesocyclone, owing to incomplete data in all three cases in the critical lowest ~100 m in the region immediately north of the mesocyclone. However, it is plausible that the baroclinically generated horizontal vorticity would have been at least partly converted to streamwise vorticity via the riverbend effect (Adlerman et al. 1999; Davies-Jones et al. 2001; Markowski and Richardson 2014) given the leftward bending of the storm-relative streamlines[4] immediately north of the low-level mesocyclones.

---

[4] The curvature of the trajectories is what matters, but it is assumed that the streamlines and trajectories both have similar curvature given that the supercell's large-scale airflow is quasi-steady (Davies-Jones 2015).

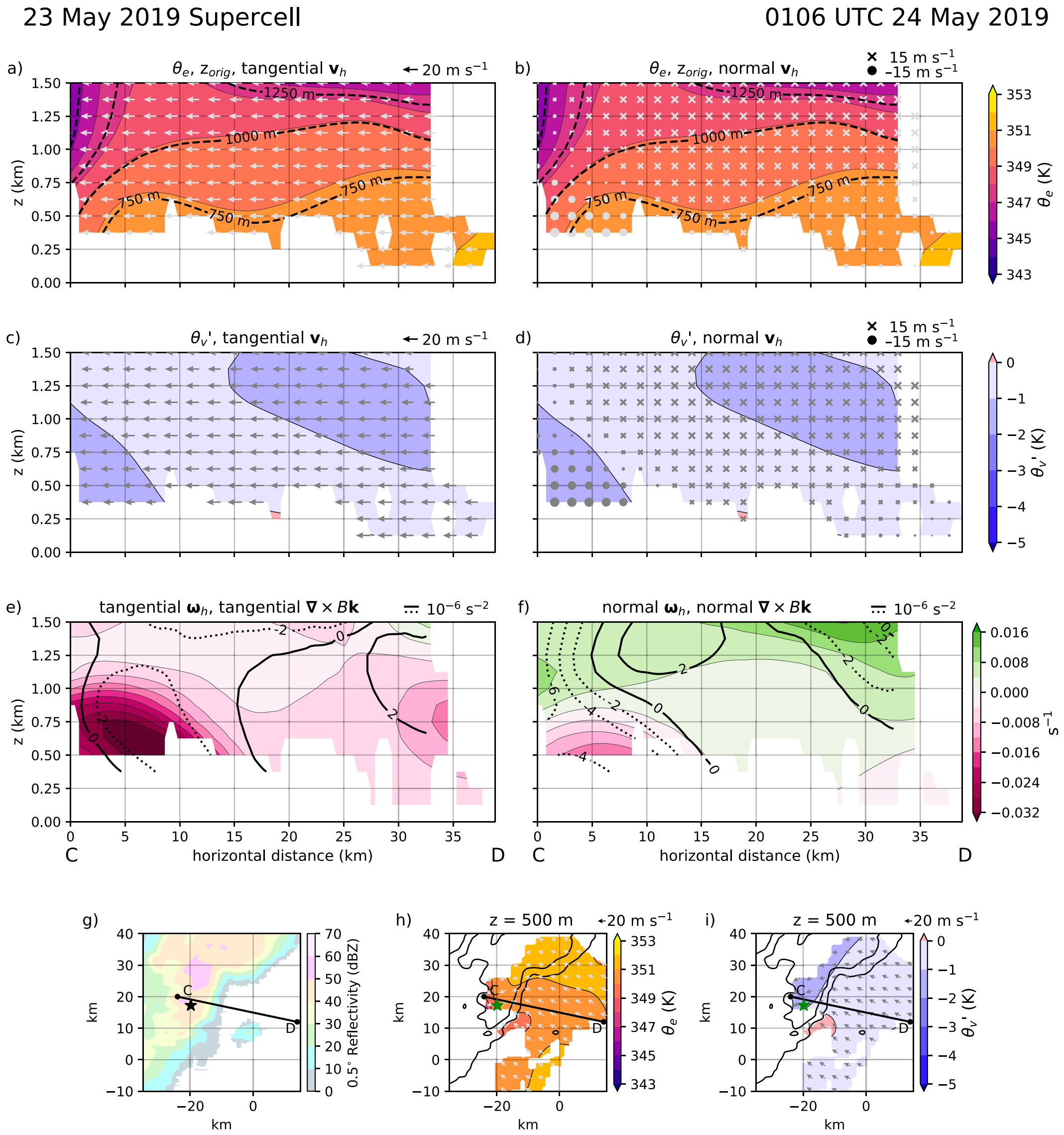

FIG. 19. As in Fig. 14, but for vertical cross section CD through the 23 May 2019 supercell. The cross section extends from northwest of the midlevel mesocyclone to the environment to the east-southeast. Reflectivity imagery from the KDDC WSR-88D at the reference time (0106 UTC 24 May) is shown in (g)–(i), and the location of the midlevel mesocyclone is indicated by a black star in (g) and green star in (h) and (i). The mesocyclone's location is determined from 0.5° elevation WSR-88D velocity data that intersect the storm at ~3.0 km above radar level.

Last, some pockets in which small (<1 K) θ_v excesses are analyzed appear at z = 1500 m in the 20 May storm (Figs. 27g–i) and at z = 500–750 m and z = 1500 m in the 23 May storm (Figs. 25d–i and 28g–i). In the 20 May storm, the location and altitude of the warm anomaly strongly suggests that it represents the main updraft of the supercell (it also is collocated with strong cyclonic curvature in the horizontal wind field). A vertical cross section through the mesocyclone area in this storm also indicates that the less negatively (and slight positively) buoyant air coincides well with the upward plume of the lower z_{orig} and higher θ_e values (cf. Figs. 17c,d and Figs. 17a,b)—a further indication of the main updraft. In the 23 May storm, however, interpretation of the warm pockets is problematic. The lower of the two pockets vanishes above 750 m (the warm pocket at 1500 m is 10 km farther east and not connected to the warm pocket in the 500–750-m layer) and is below the height of the level of free convection based on nearby soundings (not shown). The warm pocket at 1500 m is on the edge of the data and 15 km southeast (i.e., a bit far) from the midlevel mesocyclone. It seems most likely that both positive θ_v anomalies in the 23 May analysis are the result of either noisy data or a small mis-specification of $\overline{\theta}_v$.

5. Summary and future work

Over the past 40 years, numerical simulations have produced considerable evidence of the importance of baroclinic

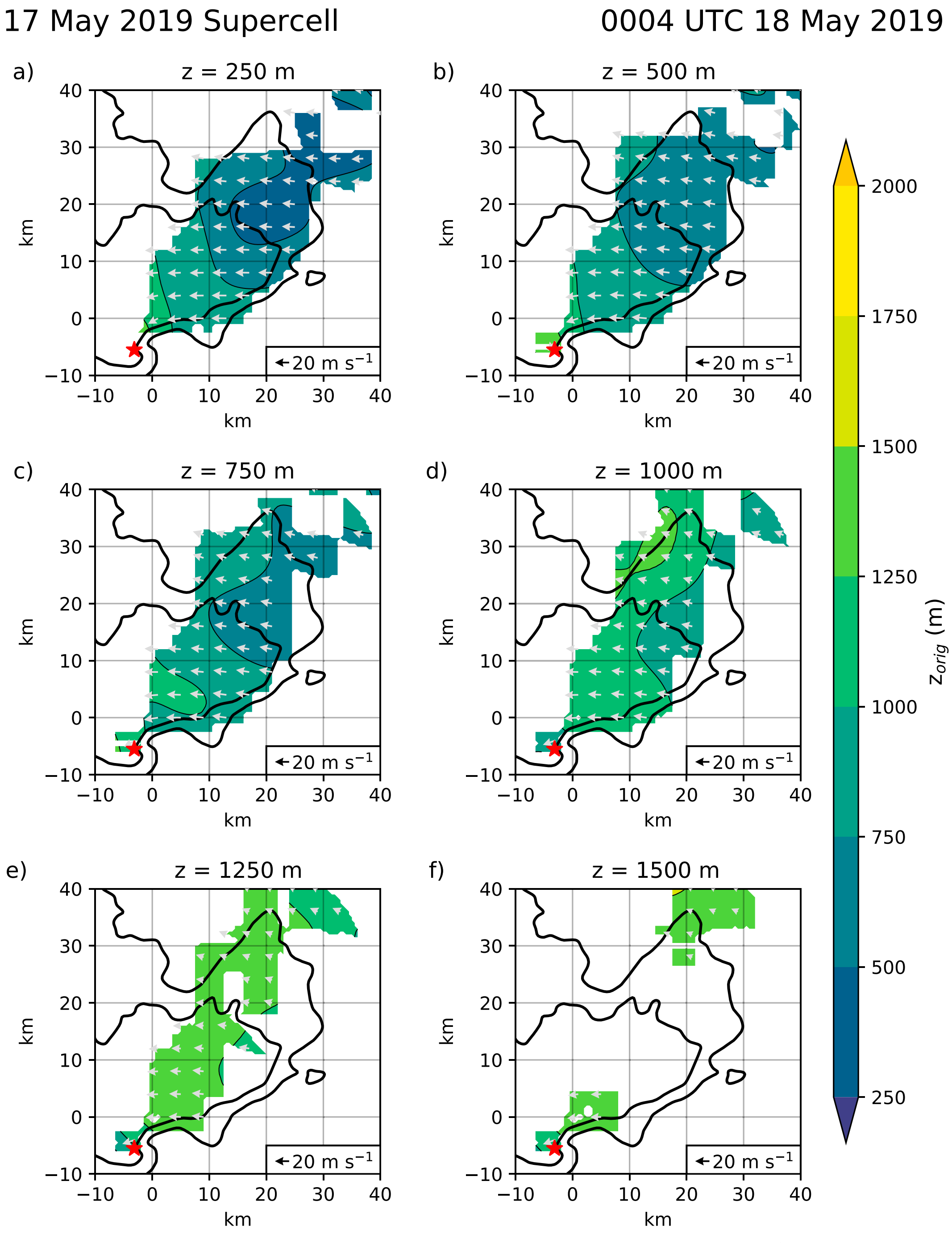

FIG. 20. Horizontal cross sections of z_{orig} (shading; m) and storm-relative winds (vectors; m s^{-1}) in the 17 May 2019 supercell at (a) 250, (b) 500, (c) 750, (d) 1000, (e) 1250, and (f) 1500 m. Although the vertical grid spacing is 125 m, every other level is omitted for brevity. Wind vectors are plotted every 4 km, and the smoothed 20- and 40-dB*Z* reflectivity contours from the KLNX WSR-88D at the reference time (0004 UTC 18 May) are plotted as thick black lines. The midlevel mesocyclone's location (red star) is determined from 0.5° elevation WSR-88D velocity data that intersect the storm at ~2.5 km above radar level.

vorticity and circulation generation in tornadogenesis in supercell storms. Perhaps surprisingly, the tale told by such simulations remains largely unobserved to date, owing to the difficulty in obtaining reliable, volumetric thermodynamic measurements, particularly in precipitation, which is where the most important baroclinity tends to be found. Moreover, recent numerical simulations with a semi-slip lower boundary condition have presented a potential alternative

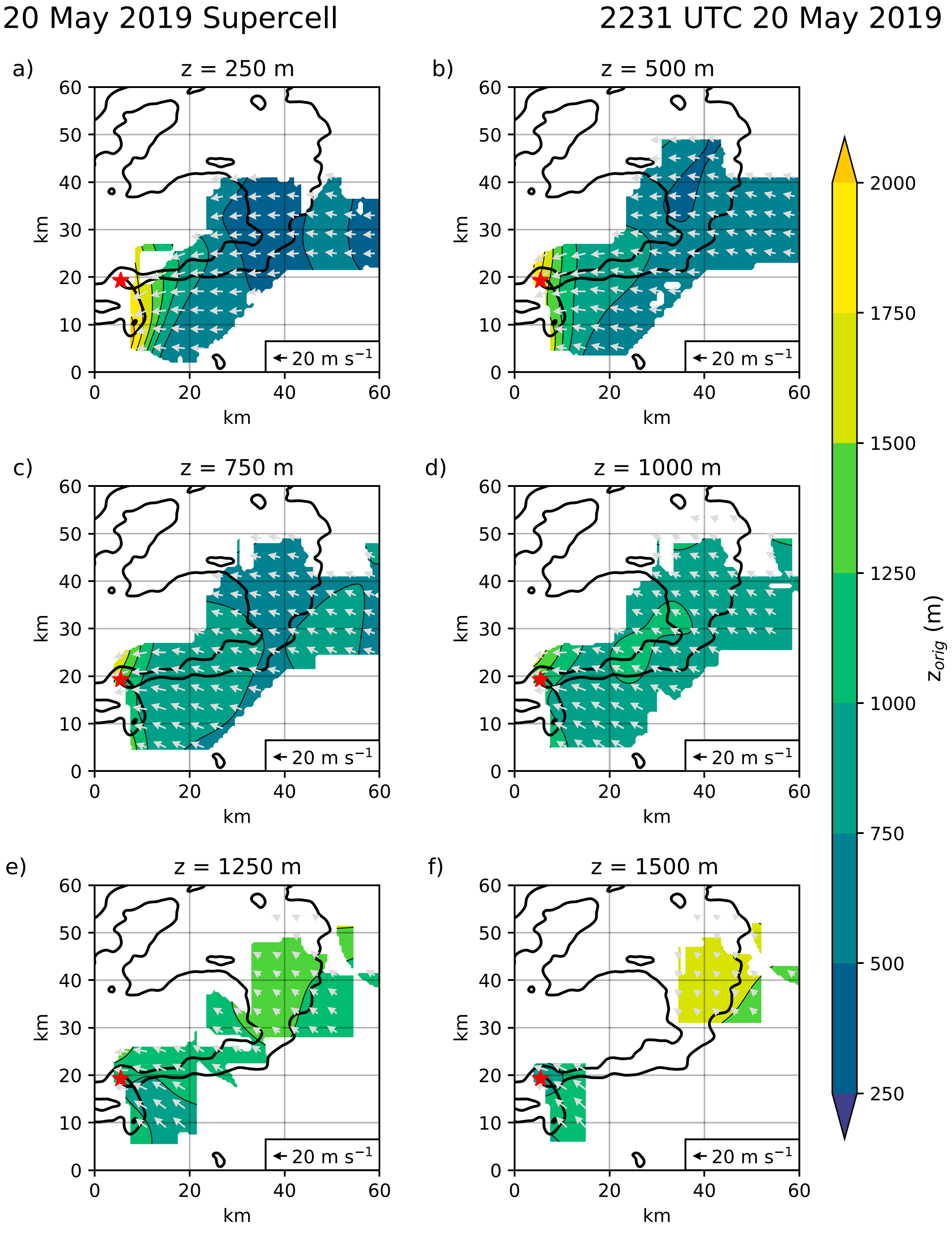

FIG. 21. As in Fig. 20, but for the 20 May 2019 supercell. The smoothed 20- and 40-dBZ reflectivity contours from the KFDR WSR-88D at the reference time (2142 UTC 20 May) are plotted as thick black lines. The midlevel mesocyclone's location (red star) is determined from 0.5° elevation WSR-88D velocity data that intersect the storm at ~1.0 km above radar level.

or complementary mechanism for tornadogenesis under certain conditions.

The pressing need to obtain thermodynamic observations within storms motivated this study, which presented analyses of the 3D thermodynamic characteristics of three tornadic supercell thunderstorms sampled by swarms of balloon-borne sondes in May 2019. These analyses are believed to be the first gridded 3D thermodynamic analyses obtained in convective storms from in situ observations. The principal findings are summarized below:

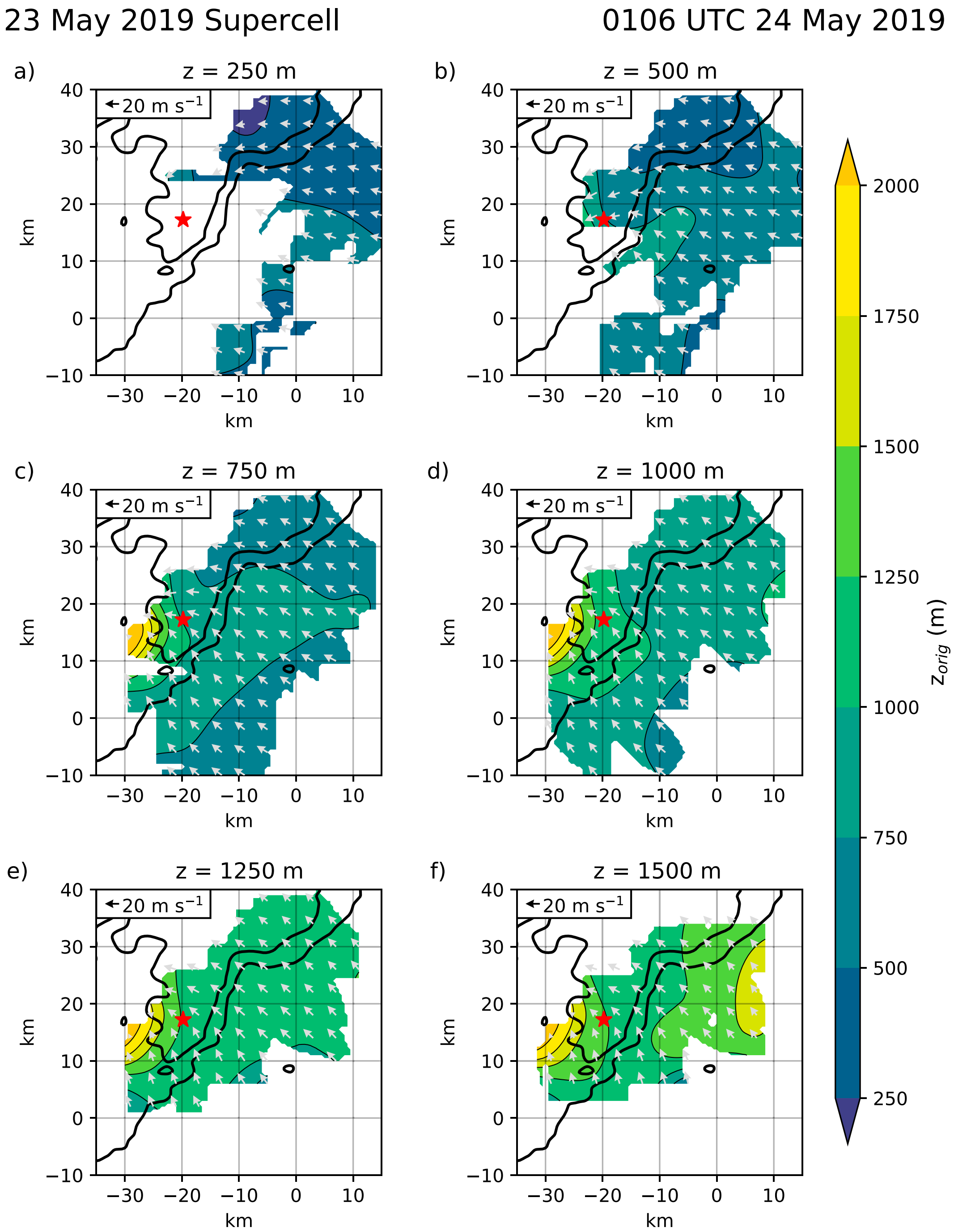

FIG. 22. As in Fig. 20, but for the 23 May 2019 supercell. The smoothed 20- and 40-dBZ reflectivity contours from the KDDC WSR-88D at the reference time (0004 UTC 18 May) are plotted as thick black lines. The midlevel mesocyclone's location (red star) is determined from 0.5° elevation WSR-88D velocity data that intersect the storm at ~3.0 km above radar level.

- The θ_e deficits observed within the outflow at the lowest grid levels (typically north and west of the low-level mesocyclones) were comparable to those observed at the surface in previously studied tornadic supercells. The largest θ_e deficits were found near the surface.
- Downward displacements of air parcels within the outflow, inferred from comparing θ_e observations in the outflow to those in the environment (and assuming θ_e conservation), were small (generally <200 m) within the forward-flank outflow and much larger (1–2 km) within the rear-flank outflow.

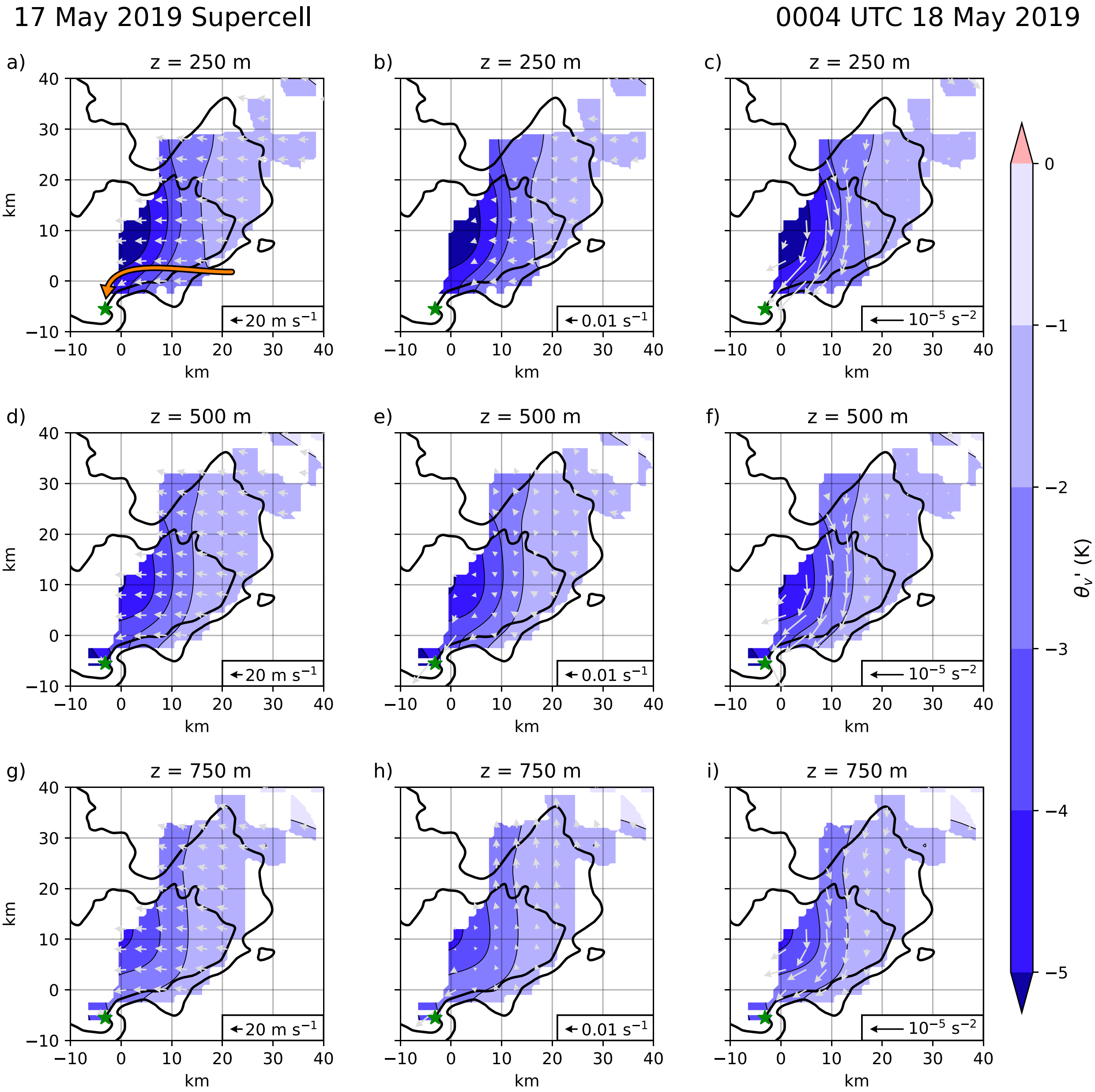

FIG. 23. Horizontal cross sections of θ'_v (shading; K) in the 17 May 2019 supercell at (a)–(c) 250, (d)–(f) 500, and (g)–(i) 750 m. Vectors represent (a),(d),(g) storm-relative winds (m s^{-1}); (b),(e),(h) horizontal vorticity ($\boldsymbol{\omega}_h$; s^{-1}); and (c),(f),(i) baroclinic horizontal vorticity generation rate (10^{-5} s^{-2}) and are plotted every 4 km. The smoothed 20- and 40-dB*Z* reflectivity contours from the KLNX WSR-88D at the reference time (0004 UTC 18 May) are also shown (thick black contours). The location of the midlevel mesocyclone is indicated by a green star, and the envisioned trajectory of an air parcel bound for the low-level mesocyclone is indicated by the orange arrow in (a). The midlevel mesocyclone's location is determined from 0.5° elevation WSR-88D velocity data that intersect the storm at ~2.5 km above radar level.

- The largest θ_v deficits observed at the lowest grid levels (typically north of the low-level mesocyclones in the regions of heaviest precipitation) also were comparable to those observed at the surface in previously studied tornadic supercells. However, in one of the tornadic supercells intercepted (17 May), the largest θ_v deficits observed at the lowest grid levels were on the cooler end of the tornadic supercell outflow spectrum. (Though negative buoyancy is implied by a θ_v deficit, the total negative buoyancy is unknown given the lack of hydrometeor mixing ratio observations.)
- In two of the supercells (17 and 20 May), θ_v deficits of 1–2 K extend to the top of sampled data regions at 1.25–1.5 km. In the third supercell (23 May), the outflow depth could

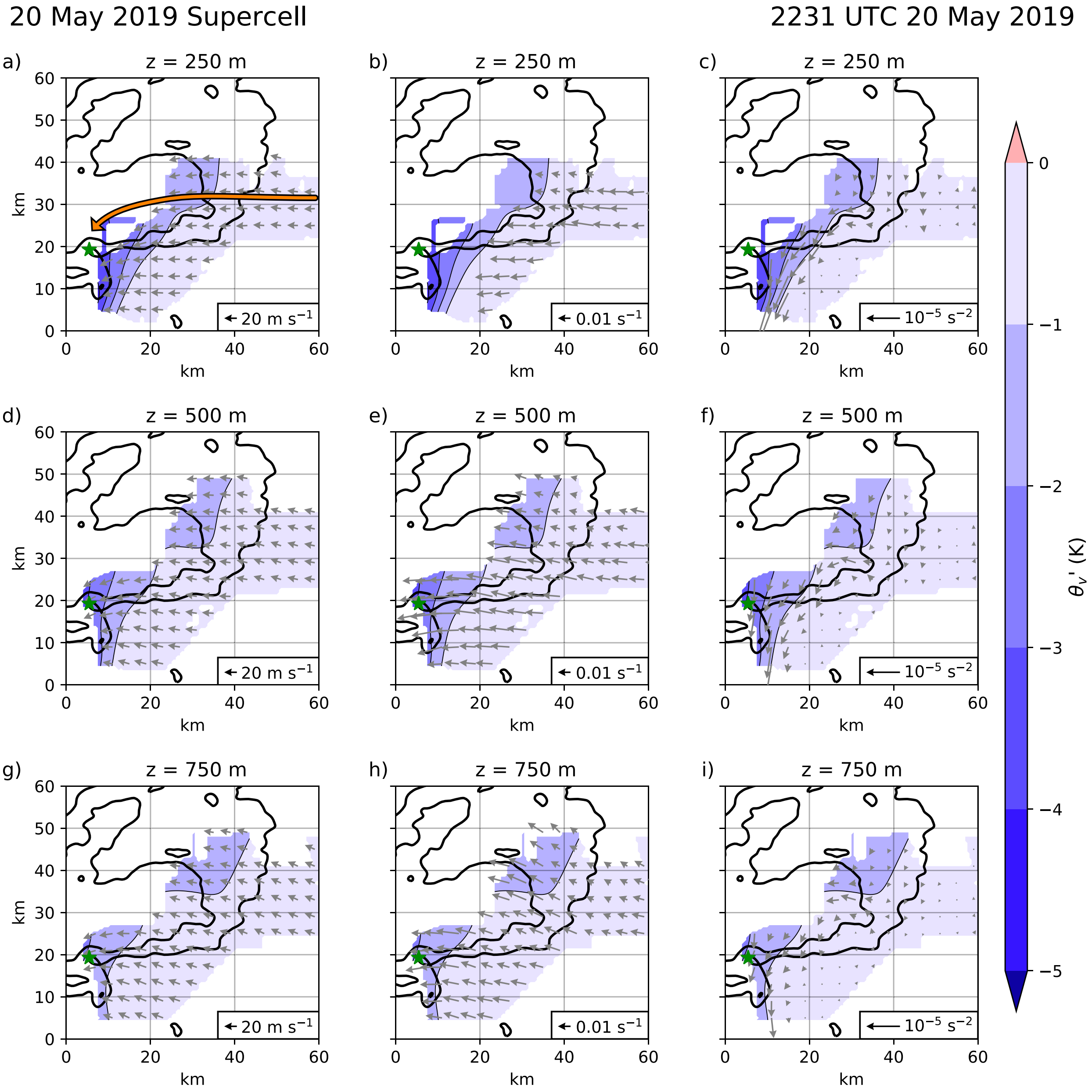

FIG. 24. As in Fig. 23, but for the 20 May 2019 supercell. The smoothed 20- and 40-dB*Z* reflectivity contours (thick black contours) are from the KFDR WSR-88D at 2231 UTC 20 May. The location of the midlevel mesocyclone is indicated by a green star, and the envisioned trajectory of an air parcel bound for the low-level mesocyclone is indicated by the orange arrow in (a). The midlevel mesocyclone's location is determined from 0.5° elevation WSR-88D velocity data that intersect the storm at ~1.0 km above radar level.

not be determined. In all three cases, however, the most significant baroclinity that would have been encountered by air parcels en route to the tornadoes spanned the lowest 750 m.

- In the two best-sampled cases (17 and 20 May), air parcels following paths toward the low-level mesocyclone pass through horizontal buoyancy gradients estimated to be capable of baroclinically generating horizontal vorticity having a magnitude of $6\text{–}10 \times 10^{-3}\ \mathrm{s}^{-1}$. A substantial component of the baroclinically generated vorticity is initially crosswise, though the vorticity subsequently could become streamwise given the leftward-bending of the airstream in which the vorticity is generated.

Additional work is needed to further understand supercell thermodynamics and the processes of tornadogenesis. The present study's findings can be integrated with the TORUS project's complementary observations from instruments such as mobile radars, UASs, mobile mesonets, and other upper-air soundings to provide a better context for the storms'

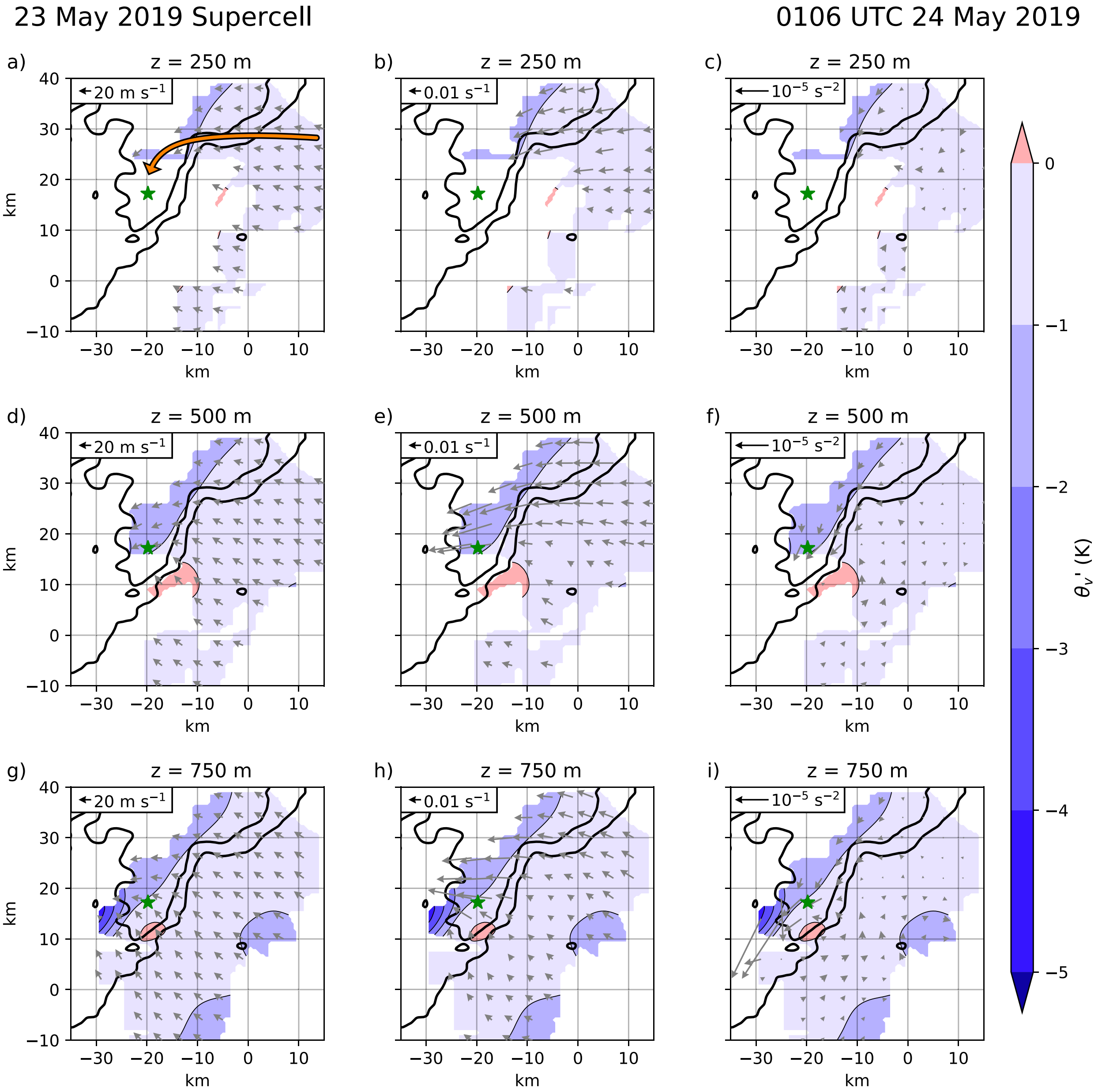

FIG. 25. As in Fig. 23, but for the 23 May 2019 supercell. The smoothed 20- and 40-dB*Z* reflectivity contours (thick black contours) are from the KDDC WSRR-88D at 0106 UTC 24 May. The location of the midlevel mesocyclone is indicated by a green star, and the envisioned trajectory of an air parcel bound for the low-level mesocyclone is indicated by an orange arrow in (a). The midlevel mesocyclone's location is determined from 0.5° elevation WSR-88D velocity data that intersect the storm at ∼3.0 km above radar level.

thermodynamic fields. For example, our 3D thermodynamic observations can be combined with 3D wind retrievals from dual-Doppler analyses. Specifically, the diabatic Lagrangian analysis (DLA) technique of Ziegler et al. (2007) and Ziegler (2013a,b) could propagate the thermodynamic data throughout portions of the storm not directly sampled by the sondes. DLA could potentially facilitate the retrieval of 4D (i.e., time-varying 3D) thermodynamic analyses. Such analyses could allow us to analyze baroclinic circulation generation about material circuits a la Rotunno and Klemp (1985). Given the aforementioned possible influence of surface friction on tornado formation (e.g., Schenkman et al. 2012, 2014; Roberts et al. 2016; Yokota et al. 2018; Roberts et al. 2020), material circuit analysis may also allow us to estimate, as a residual, frictionally induced circulation from observations of the baroclinically generated circulation and the total circulation. More thorough sampling within additional supercells in future field work could allow for a better temporal resolution of a storm's 3D thermodynamic structure as well. Moreover, current and future aboveground thermodynamic observations could be

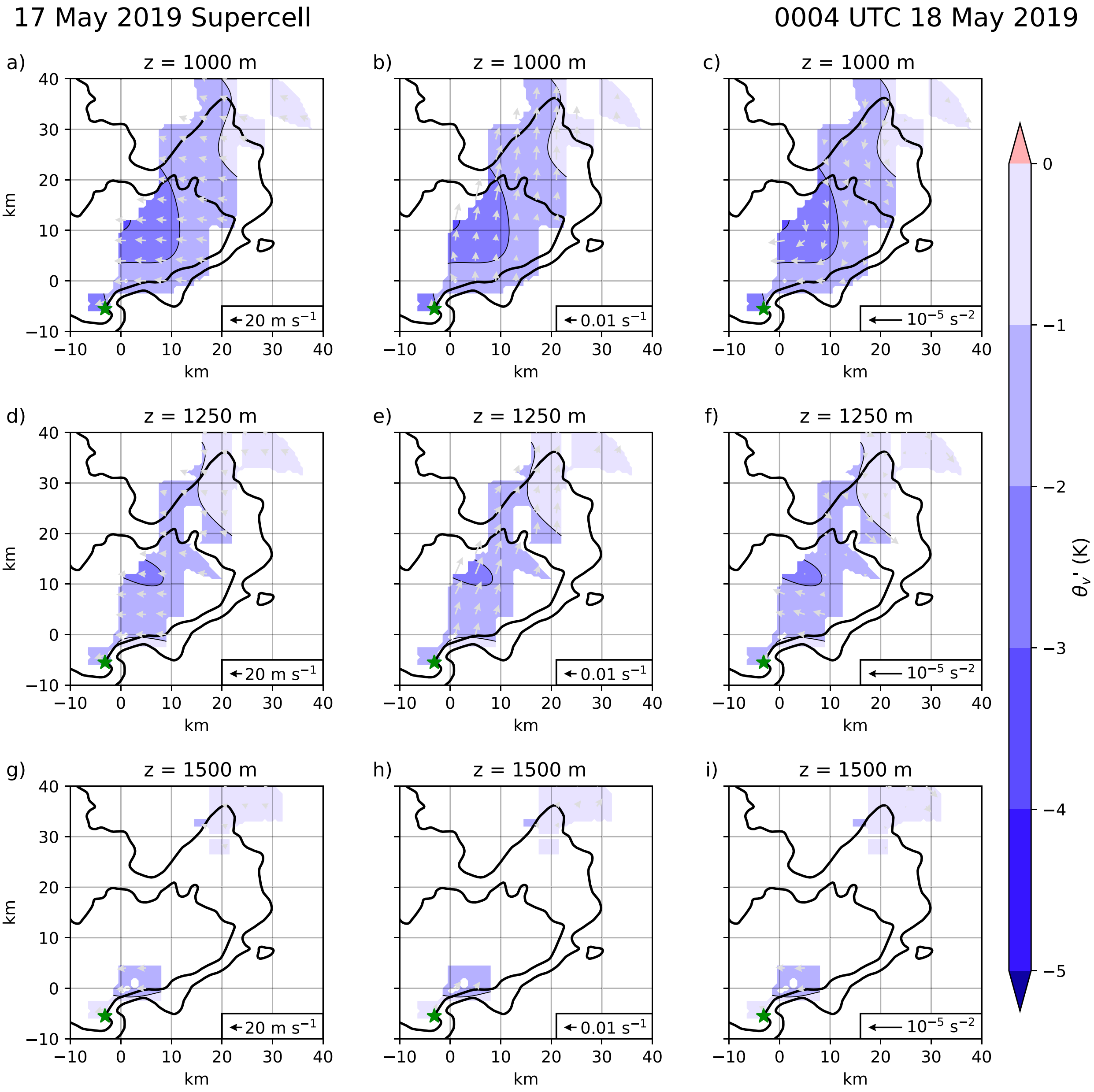

FIG. 26. As in Fig. 23, but for the 17 May 2019 supercell at the z = (a)–(c) 1000-, (d)–(f) 1250-, and (g)–(i) 1500-m grid levels. The smoothed 20- and 40-dBZ reflectivity contours from the KLNX WSR-88D at the reference time (0004 UTC 18 May) are also shown (thick black contours). The midlevel mesocyclone's location (green star) is determined from 0.5° elevation WSR-88D velocity data that intersect the storm at ~2.5 km above radar level.

assimilated into numerical simulations of supercells and used to evaluate which microphysics schemes produce a supercell with buoyancy gradients most consistent with observed aboveground thermodynamic structures of supercells (e.g., Marquis et al. 2014; Dawson et al. 2015).

The present study is not without limitations. The biggest error source is probably the long-duration time-to-space conversion, which is difficult to quantify (the fields of Δt and $\sigma_{\Delta t}$ at least help empower the reader to make their own qualitative assessments about the credibility the analyses). The long duration was necessary in order to obtain a sufficiently dense 3D distribution of observations, but the trade-off is obviously a limited ability to depict storm evolution. The rather "conservative" degree of smoothing applied in the objective analyses should mitigate against some of the error sources. Quantifying the propagation of time-to-space-conversion and instrument errors (including possible errors related to response times) into the objective analyses requires a synthetic data study with analyses based on simulating sondes traveling through a numerically simulated storm. Preliminary

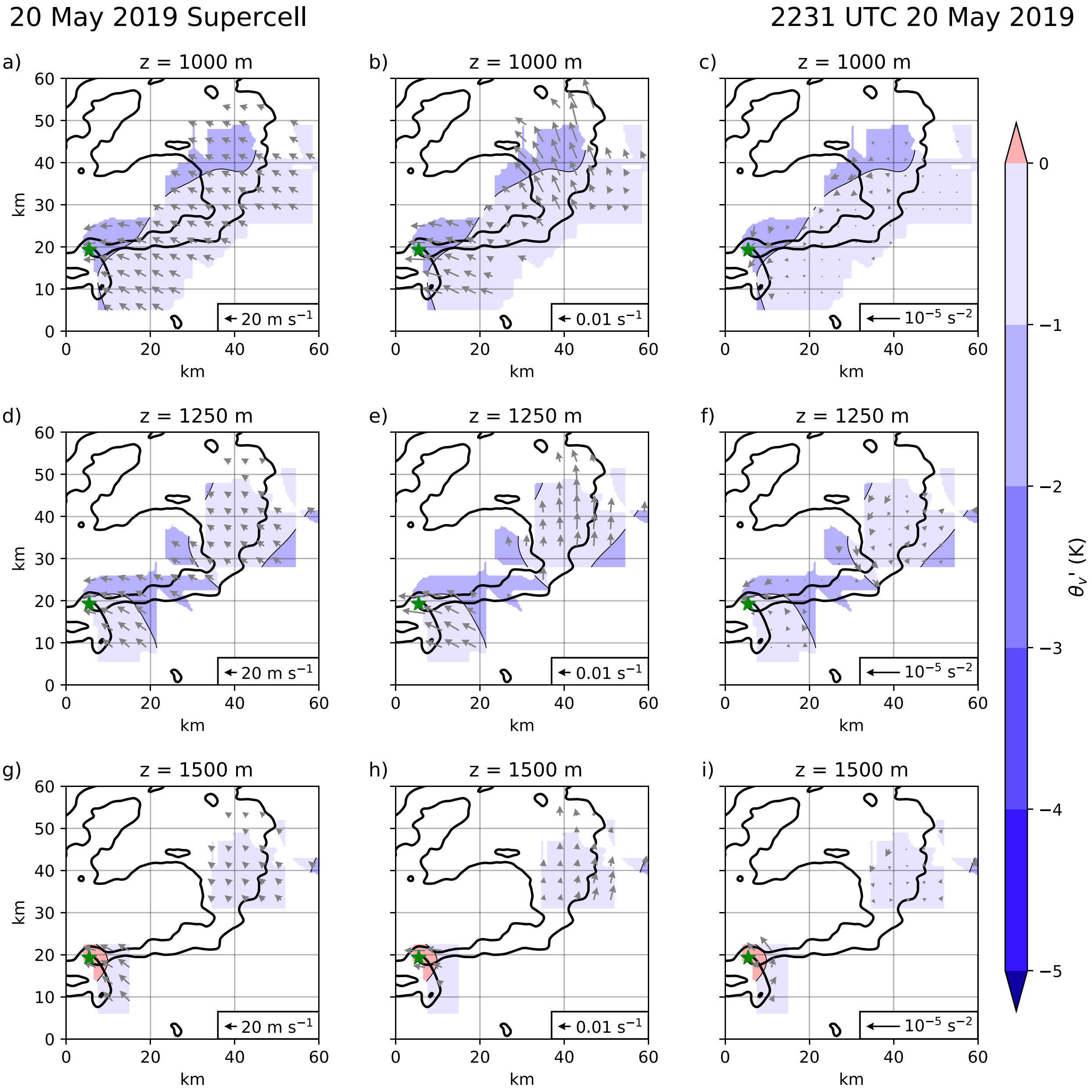

FIG. 27. As in Fig. 23, but for the 20 May 2019 supercell at the z = (a)–(c) 1000, (d)–(f) 1250, and (g)–(i) 1500-m grid levels. The smoothed 20- and 40-dBZ reflectivity contours from the KFDR WSR-88D at the reference time (2231 UTC 20 May) are also shown (thick black contours). The midlevel mesocyclone's location (green star) is determined from 0.5° elevation WSR-88D velocity data that intersect the storm at ~1.0 km above radar level.

results from such a study using a simulation from Markowski (2020) are encouraging, suggesting the root-mean-square error (RMSE) in θ_v could be well below 1 K at every level, whereas the RMSE in θ_e may be larger. Even a doubling of response times (~10, ~16, and ~0.08 s for temperature, RH, and pressure, respectively) has almost no perceivable influence on the Barnes objective analyses, given the high degree of smoothing employed and the relatively slow change in the input signal. These preliminary results do not include the effect of wet-bulb errors that are most likely to occur on the edges of the storm when sondes travel out of precipitation regions. Instrument intercomparison experiments in a controlled environment would also be beneficial to determine the magnitude of possible wet-bulbing errors. Both types of studies are warranted in the future.

Despite the limitations, the present study has shown that balloon-borne sondes are a viable way of mapping a supercell's aboveground thermodynamic structure. We hope that as technologies continue to improve, such as enhanced biodegradability of sondes and balloons, large swarms of small, light-

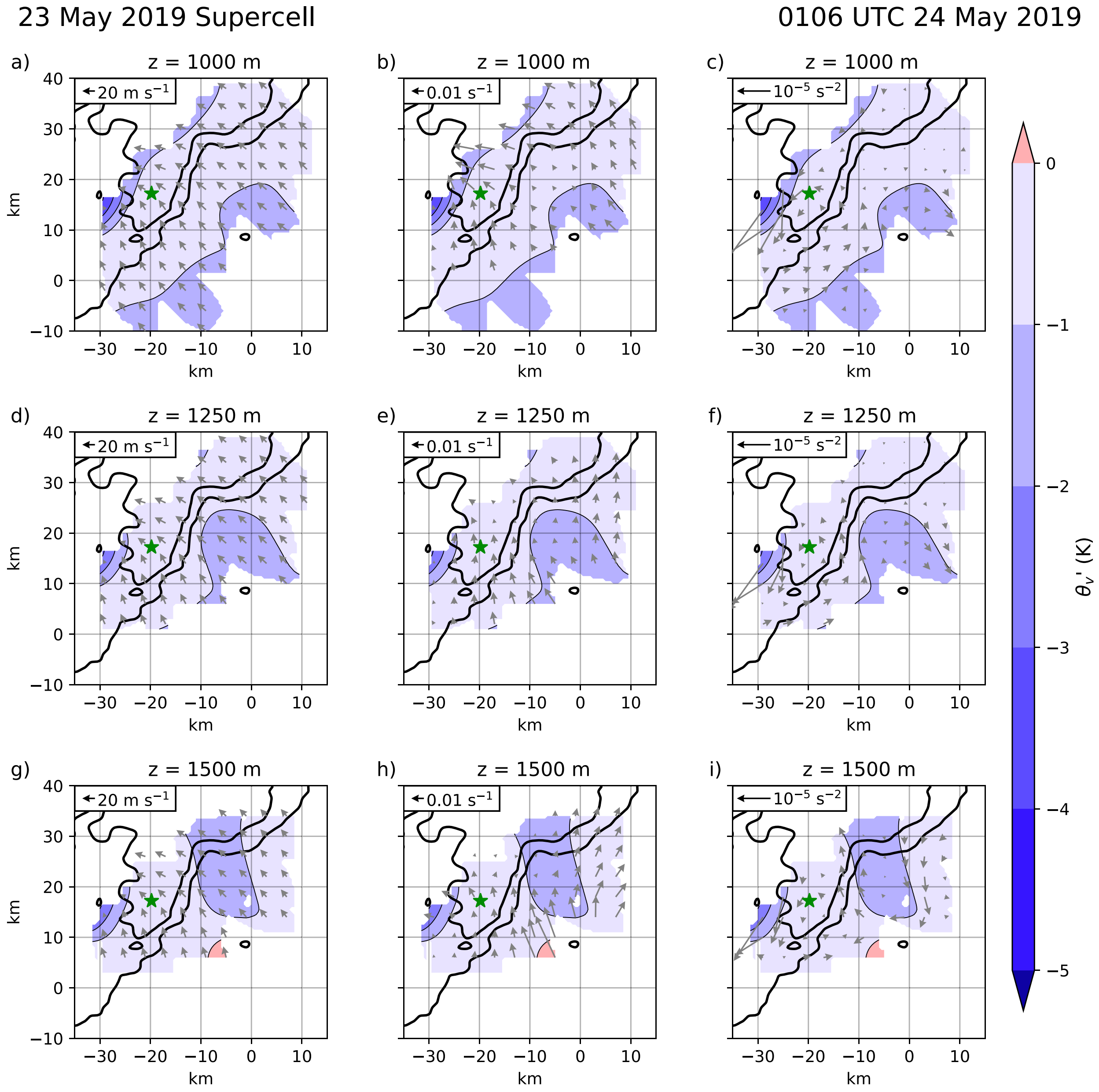

FIG. 28. As in Fig. 23, but for the 23 May 2019 supercell at the z = (a)–(c) 1000-, (d)–(f) 1250-, and (g)–(i) 1500-m grid levels. The smoothed 20- and 40-dBZ reflectivity contours from the KDDC WSR-88D at the reference time (0106 UTC 24 May) are also shown (thick black contours). The midlevel mesocyclone's location (green star) is determined from 0.5° elevation WSR-88D velocity data that intersect the storm at ~3.0 km above radar level.

weight, low-altitude sondes will become a more common method of obtaining aboveground thermodynamic observations within severe storms (with minimal environmental impact) and will continue to broaden our understanding of tornado formation.

Acknowledgments. We thank Branden Katona, Shawn Murdzek, and Dylan Steinkruger for their valuable assistance during our field project as well as beneficial conservations during post-field analysis. The TORUS team is likewise thanked for allowing our participation in their field campaign. Master's thesis committee member, Matthew Kumjian, is thanked for his feedback on earlier versions of this work, and our three anonymous reviewers are thanked for their thoughtful and constructive feedback. We are also grateful to the programmers of the Python packages MetPy (May et al. 2021) and Py-ART (Helmus and Collins 2016) as well as Anders Petersson and other developers at Sparv Embedded. Finally, this material is based upon work supported by the National Science Foundation under Grant AGS-1821885. Any opinions, findings, and conclusions or recommendations expressed in this material are those of the authors and do not necessarily reflect the views of the National Science Foundation.

Data availability statement. Data and software used for this project are openly available through the Pennsylvania State University Data Commons at https://doi.org/10.26208/67ae-sr76.

REFERENCES

Adlerman, E. J., K. K. Droegemeier, and R. Davies-Jones, 1999: A numerical simulation of cyclic mesocyclogenesis. *J. Atmos. Sci.*, **56**, 2045–2069, https://doi.org/10.1175/1520-0469(1999)056<2045:ANSOCM>2.0.CO;2.

Barnes, S. L., 1964: A technique for maximizing details in numerical weather map analysis. *J. Appl. Meteor.*, **3**, 396–409, https://doi.org/10.1175/1520-0450(1964)003<0396:ATFMDI>2.0.CO;2.

Beck, J., and C. Weiss, 2013: An assessment of low-level baroclinity and vorticity within a simulated supercell. *Mon. Wea. Rev.*, **141**, 649–669, https://doi.org/10.1175/MWR-D-11-00115.1.

Boyer, C. H., and J. M. L. Dahl, 2020: The mechanisms responsible for large near-surface vertical vorticity within simulated supercells and quasi-linear storms. *Mon. Wea. Rev.*, **148**, 4281–4297, https://doi.org/10.1175/MWR-D-20-0082.1.

Brandes, E. A., 1984a: Relationships between radar-derived thermodynamic variables and tornadogenesis. *Mon. Wea. Rev.*, **112**, 1033–1052, https://doi.org/10.1175/1520-0493(1984)112<1033:RBRDTV>2.0.CO;2.

——, 1984b: Vertical vorticity generation and mesocyclone sustenance in tornadic thunderstorms: The observational evidence. *Mon. Wea. Rev.*, **112**, 2253–2269, https://doi.org/10.1175/1520-0493(1984)112<2253:VVGAMS>2.0.CO;2.

Dahl, J. M., 2015: Near-ground rotation in simulated supercells: On the robustness of the baroclinic mechanism. *Mon. Wea. Rev.*, **143**, 4929–4942, https://doi.org/10.1175/MWR-D-15-0115.1.

Davies-Jones, R., 2015: A review of supercell and tornado dynamics. *Atmos. Res.*, **158–159**, 274–291, https://doi.org/10.1016/j.atmosres.2014.04.007.

——, and H. Brooks, 1993: Mesocyclogenesis from a theoretical perspective. *The Tornado: Its Structure, Dynamics, Prediction, and Hazards, Geophys. Monogr.*, Vol. 79, Amer. Geophys. Union, 104–114, https://doi.org/10.1029/GM079p0105.

——, R. J. Trapp, and H. B. Bluestein, 2001: Tornadoes and tornadic storms. *Severe Convective Storms*, Meteor. Monogr., No. 50, Amer. Meteor. Soc., 167–222, https://doi.org/10.1175/0065-9401-28.50.167.

Dawson, D. T., M. Xue, J. A. Milbrandt, and A. Shapiro, 2015: Sensitivity of real-data simulations of the 3 May 1999 Oklahoma City tornadic supercell and associated tornadoes to multimoment microphysics. Part I: Storm- and tornado-scale numerical forecasts. *Mon. Wea. Rev.*, **143**, 2241–2265, https://doi.org/10.1175/MWR-D-14-00279.1.

Frew, E. W., B. Argrow, S. Borenstein, S. Swenson, C. A. Hirst, H. Havenga, and A. Houston, 2020: Field observation of tornadic supercells by multiple autonomous fixed-wing unmanned aircraft. *J. Field Robot.*, **37**, 1077–1093, https://doi.org/10.1002/rob.21947.

Fujita, T., 1955: Results of detailed synoptic studies of squall lines. *Tellus*, **7**, 405–436, https://doi.org/10.1111/j.2153-3490.1955.tb01181.x.

Gal-Chen, T., 1978: A method for the initialization of the anelastic equations: Implications for matching models with observations. *Mon. Wea. Rev.*, **106**, 587–606, https://doi.org/10.1175/1520-0493(1978)106<0587:AMFTIO>2.0.CO;2.

Gilmore, M. S., and L. J. Wicker, 1998: The influence of midtropospheric dryness on supercell morphology and evolution. *Mon. Wea. Rev.*, **126**, 943–958, https://doi.org/10.1175/1520-0493(1998)126<0943:TIOMDO>2.0.CO;2.

Grzych, M. L., B. D. Lee, and C. A. Finley, 2007: Thermodynamic analysis of supercell rear-flank downdrafts from project ANSWERS. *Mon. Wea. Rev.*, **135**, 240–246, https://doi.org/10.1175/MWR3288.1.

Guarriello, F., C. J. Nowotarski, and C. C. Epifanio, 2018: Effects of the low-level wind profile on outflow position and near-surface vertical vorticity in simulated supercell thunderstorms. *J. Atmos. Sci.*, **75**, 731–753, https://doi.org/10.1175/JAS-D-17-0174.1.

Hane, C. E., and P. S. Ray, 1985: Pressure and buoyancy fields derived from Doppler radar data in a tornadic thunderstorm. *J. Atmos. Sci.*, **42**, 18–35, https://doi.org/10.1175/1520-0469(1985)042<0018:PABFDF>2.0.CO;2.

Hauser, D., F. Roux, and P. Amayenc, 1988: Comparison of two methods for the retrieval of thermodynamic and microphysical variables from Doppler radar measurements: Application to the case of a tropical squall line. *J. Atmos. Sci.*, **45**, 1285–1303, https://doi.org/10.1175/1520-0469(1988)045<1285:COTMFT>2.0.CO;2.

Helmus, J. J., and S. M. Collins, 2016: The Python ARM Radar Toolkit (Py-ART), a library for working with weather radar data in the Python programming language. *J. Open Res. Software*, **4**, e25, https://doi.org/10.5334/jors.119.

Hirth, B. D., J. L. Schroeder, and C. C. Weiss, 2008: Surface analysis of the rear-flank downdraft outflow in two tornadic supercells. *Mon. Wea. Rev.*, **136**, 2344–2363, https://doi.org/10.1175/2007MWR2285.1.

Houston, A. L., R. J. Laurence, T. W. Nichols, S. Waugh, B. Argrow, and C. L. Ziegler, 2016: Intercomparison of unmanned aircraftborne and mobile mesonet atmospheric sensors. *J. Atmos. Oceanic Technol.*, **33**, 1569–1582, https://doi.org/10.1175/JTECH-D-15-0178.1.

Klemp, J. B., and R. B. Wilhelmson, 1978: The simulation of three-dimensional convective storm dynamics. *J. Atmos. Sci.*, **35**, 1070–1096, https://doi.org/10.1175/1520-0469(1978)035<1070:TSOTDC>2.0.CO;2.

——, and R. Rotunno, 1983: A study of the tornadic region within a supercell thunderstorm. *J. Atmos. Sci.*, **40**, 359–377, https://doi.org/10.1175/1520-0469(1983)040<0359:ASOTTR>2.0.CO;2.

——, R. B. Wilhelmson, and P. S. Ray, 1981: Observed and numerically simulated structure of a mature supercell thunderstorm. *J. Atmos. Sci.*, **38**, 1558–1580, https://doi.org/10.1175/1520-0469(1981)038<1558:OANSSO>2.0.CO;2.

Kosiba, K., J. Wurman, Y. Richardson, P. Markowski, P. Robinson, and J. Marquis, 2013: Genesis of the Goshen County, Wyoming, tornado on 5 June 2009 during VORTEX2. *Mon. Wea. Rev.*, **141**, 1157–1181, https://doi.org/10.1175/MWR-D-12-00056.1.

Ludlam, F. H., 1963: Severe local storms: A review. *Severe Local Storms*, Meteor. Monogr., No. 5, Amer. Meteor. Soc., 1–32.

Majcen, M., P. Markowski, Y. Richardson, D. Dowell, and J. Wurman, 2008: Multipass objective analyses of Doppler radar data. *J. Atmos. Oceanic Technol.*, **25**, 1845–1858, https://doi.org/10.1175/2008JTECHA1089.1.

Markowski, P. M., 2016: An idealized numerical simulation investigation of the effects of surface drag on the development of near-surface vertical vorticity in supercell thunderstorms. *J.*

Atmos. Sci., **73**, 4349–4385, https://doi.org/10.1175/JAS-D-16-0150.1.

——, 2020: What is the intrinsic predictability of tornadic supercell thunderstorms? *Mon. Wea. Rev.*, **148**, 3157–3180, https://doi.org/10.1175/MWR-D-20-0076.1.

——, and G. H. Bryan, 2016: LES of laminar flow in the PBL: A potential problem for convective storm simulations. *Mon. Wea. Rev.*, **144**, 1841–1850, https://doi.org/10.1175/MWR-D-15-0439.1.

——, and Y. P. Richardson, 2009: Our current understanding, forecasting considerations, and questions to guide future research. *Atmos. Res.*, **93**, 3–10, https://doi.org/10.1016/j.atmosres.2008.09.015.

——, and ——, 2014: The influence of environmental low-level shear and cold pools on tornadogenesis: Insights from idealized simulations. *J. Atmos. Sci.*, **71**, 243–275, https://doi.org/10.1175/JAS-D-13-0159.1.

——, J. M. Straka, and E. N. Rasmussen, 2002: Direct surface thermodynamic observations within the rear-flank downdrafts of nontornadic and tornadic supercells. *Mon. Wea. Rev.*, **130**, 1692–1721, https://doi.org/10.1175/1520-0493(2002)130<1692:DSTOWT>2.0.CO;2.

——, Y. Richardson, E. Rasmussen, J. Straka, R. Davies-Jones, and R. J. Trapp, 2008: Vortex lines within low-level mesocyclones obtained from pseudo-dual-Doppler radar observations. *Mon. Wea. Rev.*, **136**, 3513–3535, https://doi.org/10.1175/2008MWR2315.1.

——, M. Majcen, Y. Richardson, J. Marquis, and J. Wurman, 2011: Characteristics of the wind field in three nontornadic low-level mesocyclones observed by the Doppler on Wheels radars. *Electron. J. Severe Storms Meteor.*, **6**(3), 1–48.

——, and Coauthors, 2012a: The pretornadic phase of the Goshen County, Wyoming, supercell of 5 June 2009 intercepted by VORTEX2. Part I: Evolution of kinematic and surface thermodynamic fields. *Mon. Wea. Rev.*, **140**, 2887–2915, https://doi.org/10.1175/MWR-D-11-00336.1.

——, and Coauthors, 2012b: The pretornadic phase of the Goshen County, Wyoming, supercell of 5 June 2009 intercepted by VORTEX2. Part II: Intensification of low-level rotation. *Mon. Wea. Rev.*, **140**, 2915–2938, https://doi.org/10.1175/MWR-D-11-00337.1.

——, T. Hatlee, and Y. Richardson, 2018a: Tornadogenesis in the 12 May 2010 supercell thunderstorm intercepted by VORTEX2 near Clinton, Oklahoma. *Mon. Wea. Rev.*, **146**, 3623–3650, https://doi.org/10.1175/MWR-D-18-0196.1.

——, Y. P. Richardson, S. H. Richardson, and A. Petersson, 2018b: Aboveground thermodynamic observations in convective storms from balloonborne probes acting as pseudo-Lagrangian drifters. *Bull. Amer. Meteor. Soc.*, **99**, 711–724, https://doi.org/10.1175/BAMS-D-17-0204.1.

Marquis, J., Y. Richardson, P. Markowski, D. Dowell, and J. Wurman, 2012: Tornado maintenance investigated with high-resolution dual-Doppler and EnKF analysis. *Mon. Wea. Rev.*, **140**, 3–27, https://doi.org/10.1175/MWR-D-11-00025.1.

——, ——, ——, ——, ——, K. Kosiba, P. Robinson, and G. Romine, 2014: An investigation of the Goshen County, Wyoming, tornadic supercell of 5 June 2009 using EnKF assimilation of mobile mesonet and radar observations collected during VORTEX2. Part I: Experiment design and verification of the EnKF analyses. *Mon. Wea. Rev.*, **142**, 530–554, https://doi.org/10.1175/MWR-D-13-00007.1.

May, R. M., S. C. Arms, P. Marsh, E. Bruning, J. R. Leeman, K. Goebbert, J. E. Thielen, and Z. S. Bruick, 2021: Metpy: A Python package for meteorological data. Unidata, Accessed 30 April 2021, https://github.com/Unidata/MetPy.

NOAA/NCEI, 2021: National Centers for Environmental Information (NCEI) storm events database. Accessed 1 May 2021, https://www.ncdc.noaa.gov/stormevents/.

Parker, M. D., and J. M. Dahl, 2015: Production of near-surface vertical vorticity by idealized downdrafts. *Mon. Wea. Rev.*, **143**, 2795–2816, https://doi.org/10.1175/MWR-D-14-00310.1.

Pauley, P. M., and X. Wu, 1990: The theoretical, discrete, and actual response of the Barnes objective analysis scheme for one- and two-dimensional fields. *Mon. Wea. Rev.*, **118**, 1145–1164, https://doi.org/10.1175/1520-0493(1990)118<1145:TTDAAR>2.0.CO;2.

Rasmussen, E. N., and J. M. Straka, 1998: Variations in supercell morphology. Part I: Observations of the role of upper-level storm-relative flow. *Mon. Wea. Rev.*, **126**, 2406–2421, https://doi.org/10.1175/1520-0493(1998)126<2406:VISMPI>2.0.CO;2.

Roberts, B., M. Xue, A. D. Schenkman, and D. T. Dawson, 2016: The role of surface drag in tornadogenesis within an idealized supercell simulation. *J. Atmos. Sci.*, **73**, 3371–3395, https://doi.org/10.1175/JAS-D-15-0332.1.

——, ——, and D. T. Dawson, 2020: The effect of surface drag strength on mesocyclone intensification and tornadogenesis in idealized supercell simulations. *J. Atmos. Sci.*, **77**, 1699–1721, https://doi.org/10.1175/JAS-D-19-0109.1.

Rotunno, R., 1993: Supercell thunderstorm modeling and theory. *The Tornado: Its Structure, Dynamics, Prediction, and Hazards*, Geophys. Monogr., Vol. 79, Amer. Geophys. Union, 57–73, https://doi.org/10.1029/GM079p0057.

——, and J. Klemp, 1985: On the rotation and propagation of simulated supercell thunderstorms. *J. Atmos. Sci.*, **42**, 271–292, https://doi.org/10.1175/1520-0469(1985)042<0271:OTRAPO>2.0.CO;2.

——, P. M. Markowski, and G. H. Bryan, 2017: "Near ground" vertical vorticity in supercell thunderstorm models. *J. Atmos. Sci.*, **74**, 1757–1766, https://doi.org/10.1175/JAS-D-16-0288.1.

Schenkman, A. D., M. Xue, and A. Shapiro, 2012: Tornadogenesis in a simulated mesovortex within a mesoscale convective system. *J. Atmos. Sci.*, **69**, 3372–3390, https://doi.org/10.1175/JAS-D-12-038.1.

——, ——, and M. Hu, 2014: Tornadogenesis in a high-resolution simulation of the 8 May 2003 Oklahoma City supercell. *J. Atmos. Sci.*, **71**, 130–154, https://doi.org/10.1175/JAS-D-13-073.1.

Shabbott, C. J., and P. M. Markowski, 2006: Surface in situ observations within the outflow of forward-flank downdrafts of supercell thunderstorms. *Mon. Wea. Rev.*, **134**, 1422–1441, https://doi.org/10.1175/MWR3131.1.

Smith, B. T., R. L. Thompson, J. S. Grams, C. Broyles, and H. E. Brooks, 2012: Convective modes for significant severe thunderstorms in the contiguous United States. Part I: Storm classification and climatology. *Wea. Forecasting*, **27**, 1114–1135, https://doi.org/10.1175/WAF-D-11-00115.1.

Straka, J. M., E. N. Rasmussen, and S. E. Fredrickson, 1996: A mobile mesonet for finescale meteorological observations. *J. Atmos. Oceanic Technol.*, **13**, 921–936, https://doi.org/10.1175/1520-0426(1996)013<0921:AMMFFM>2.0.CO;2.

Taylor, G. I., 1938: The spectrum of turbulence. *Proc. Roy. Soc. London A*, **164**, 476–490, https://doi.org/10.1098/rspa.1938.0032.

Trapp, R. J., and B. H. Fiedler, 1995: Tornado-like vortex genesis in a simplified numerical model. *J. Atmos. Sci.*, **52**, 3757–3778, https://doi.org/10.1175/1520-0469(1995)052<3757:TLVIAS>2.0.CO;2.

Wang, A., Y. Pan, and P. M. Markowski, 2020: The influence of turbulence memory on idealized tornado simulations. *Mon. Wea. Rev.*, **148**, 4875–4892, https://doi.org/10.1175/MWR-D-20-0031.1.

Waugh, S., 2020: NSSL mobile quality controlled (QC) radiosonde data, version 1.0. UCAR/NCAR–Earth Observing Laboratory, accessed 30 April 2020, https://doi.org/10.26023/MDEM-SG4J-5P10.

——, and S. E. Fredrickson, 2010: An improved aspirated temperature system for mobile meteorological observations, especially in severe weather. *25th Conf. on Severe Local Storms*, Denver, CO, Amer. Meteor. Soc., P5.2, https://ams.confex.com/ams/25SLS/webprogram/Paper176205.html.

Weiss, C. C., and J. L. Schroeder, 2008: StickNet—A new portable, rapidly-deployable, surface observing system. *24th Conf. on Interactive Information Processing Systems (IIPS)*, New Orleans, LA, Amer. Meteor. Soc., 4A.1, https://ams.confex.com/ams/pdfpapers/134047.pdf.

——, D. C. Dowell, J. L. Schroeder, P. S. Skinner, A. E. Reinhart, P. M. Markowski, and Y. P. Richardson, 2015: A comparison of near-surface buoyancy and baroclinity across three VORTEX2 supercell intercepts. *Mon. Wea. Rev.*, **143**, 2736–2753, https://doi.org/10.1175/MWR-D-14-00307.1.

Yokota, S., H. Niino, H. Seko, M. Kunii, and H. Yamauchi, 2018: Important factors for tornadogenesis as revealed by high-resolution ensemble forecasts of the Tsukuba supercell tornado of 6 May 2012 in Japan. *Mon. Wea. Rev.*, **146**, 1109–1132, https://doi.org/10.1175/MWR-D-17-0254.1.

Ziegler, C. L., 2013a: A diabatic Lagrangian technique for the analysis of convective storms. Part I: Description and validation via an observing system simulation experiment. *J. Atmos. Oceanic Technol.*, **30**, 2248–2265, https://doi.org/10.1175/JTECH-D-12-00194.1.

——, 2013b: A diabatic Lagrangian technique for the analysis of convective storms. Part II: Application to a radar-observed storm. *J. Atmos. Oceanic Technol.*, **30**, 2266–2280, https://doi.org/10.1175/JTECH-D-13-00036.1.

——, M. S. Burban, and E. N. Rasmussen, 2007: A Lagrangian objective analysis technique for assimilating in situ observations with multiple-radar-derived airflow. *Mon. Wea. Rev.*, **135**, 2417–2442, https://doi.org/10.1175/MWR3396.1.